



UNIVERSITAT POLITÈCNICA DE CATALUNYA
BARCELONATECH
Escola d'Enginyeria de Barcelona Est

BACHELOR PROJECT DEGREE

Mechanical Engineering Degree

**MECHANICAL BENCH CHARACTERIZATION FOR THE
STUDY OF HYPODERMIC NEEDLE'S BEHAVIOR IN A
SOFT-TISSUE**



Memory

Autor: Alba Bertran Segales
Director: Antonio Jose Sánchez Egea
Convocation: 01-2021

Resum

Aquest projecte, pretén ser el punt de partida d'una nova àrea de recerca en el departament d'Enginyeria Mecànica de la Universitat Politècnica de Catalunya, sobre la mecànica d'inserció d'agulles mèdiques en teixits biològics.

El present document, recull informació sobre estudis previs i avanços fets en la matèria, junt amb el disseny i caracterització d'un banc d'assajos creat a l'escola, per la realització de experiments amb diferents agulles hipodèrmiques. S'inclouen els pertinents anàlisis de funcionament i calibratges fets en la posada en marxa del prototip.

El projecte inclou la modelització del procediment experimental realitzat i el tractament de les dades extretes. En el estudi experimental, s'analitzen dos paràmetres influents en la mecànica d'inserció d'agulles hipodèrmiques en teixits biològics: el diàmetre de l'agulla i la velocitat d'inserció de l'agulla. Finalment, es descriu el comportament observat en teixit provat i es detalla de la influència dels paràmetres analitzats en els resultats obtinguts experimentalment. S'inclou un apartat on es descriuen els pròxims passos que es realitzaran en futures investigacions.

Resumen

Este proyecto, pretende ser el punto de partida de una nueva área de investigación en el Departamento de Ingeniería Mecánica de la Universidad Politécnica de Cataluña, sobre la mecánica de inserción de agujas médicas en tejidos biológicos.

El presente documento reúne, información sobre estudios previos y avances realizados en el campo, junto con el diseño y caracterización de un banco de pruebas creado en la escuela para la realización de experimentos con diferentes agujas hipodérmicas. Se incluyen también los análisis del funcionamiento y calibraciones realizadas en la puesta en marcha del prototipo.

El proyecto también incluye el modelado del procedimiento experimental realizado y el tratamiento de los datos extraídos. En el estudio experimental, se analizan dos parámetros influyentes en la mecánica de inserción de agujas hipodérmicas en tejidos biológicos: el diámetro de la aguja y la velocidad de inserción de aguja. Finalmente, se describe el comportamiento observado en el tejido probado y se detalla la influencia de los parámetros analizados en resultados obtenidos experimentalmente. Incluye una sección donde se describen los próximos pasos a seguir en futuras investigaciones.

Abstract

This project aims to be the starting point for a new research topic in the Department of Mechanical Engineering at the Polytechnic University of Catalonia, on the study of the mechanics involved when inserting medical needles into biological tissues.

The present paper gathers previous investigations and advances made in the field, together with the design and characterization of a test bench created in the school to conduct tests with different hypodermic needles, including the operational analyses and calibrations performed of the first proposed prototype.

It also includes the modelization of the experimental procedure followed, and data processing of the values extracted. In the experimental study, two influential parameters on the hypodermic needle insertion mechanics are analyzed: the needle diameter and the needle insertion speed. Finally, it is described the behavior observed in the tested tissue and detailed the influence of the parameters analyzed on the experimental results. It includes a section describing the next steps for future research.

Acknowledgements

First, I want to give huge thanks to the tutor of this project, Antonio Jose Sánchez Egea for involving me in this project, guiding me through it, and helping me with the English transcription process. His knowledge, attention and patience have been crucial to the realization of this project.

Secondly, I want to thank M^a Carme Segales Arqué of the pharmacology team of WeLab, for providing some of the material tested and its knowledge on the matters.

Lastly, I want to thank Víctor Navarro González for the free coding classes, and my family for the patience and support given.



Glossary

Arduino	Open-source electronic prototyping platform.
Bevel	A sloping edge.
CAD	Computer-aided design.
COM	Serial monitor is the 'cable' between the computer and the Arduino UNO. Allows you to send and receive text messages.
ECM	Extracellular matrix.
Gauge	Inner measurement or opening of the needle.
PVA	Polyvinyl Alcohol.
PVC	Polyvinyl chloride.
Soft Tissue	Characterize for connecting, surrounding and giving support to internal organs and bones.
Stiffness	Is the extent to which an object resists deformation in response to an applied force.
UPC	Universitat Politècnica de Catalunya.
Hypodermic	Relating to the region immediately beneath the skin.

Index

RESUM	III
RESUMEN	IV
ABSTRACT	V
ACKNOWLEDGEMENTS	VII
GLOSSARY	IX
1. PREFACE	15
1.1. Project Origin	15
1.2. Motivation	15
1.3. Requirements	15
2. SCOPE	16
2.1. Project Objectives	16
2.2. Project Scope	16
2.3. Chronogram	17
3. INTRODUCTION	18
3.1. Needle insertion mechanics	18
3.2. State of Art	20
3.2.1. Effect of needle diameter and tip geometry	20
3.2.2. Insertion speed effects	20
3.2.3. Other parameters	21
3.2.4. Test benches created for the experiments	23
3.3. Mathematical modelling of Insertion forces	26
3.3.1. Stiffness force	26
3.3.2. Friction force	28
3.3.3. Cutting force	29
3.4. Soft-Tissue Viscoelasticity	29
3.4.1. Relaxation	31
3.4.2. Creep	31
3.4.3. Hysteresis	32
3.5. Mechanical bench requirements and Test design	33
4. DESIGN AND ASSEMBLY	34
4.1. Driving Part design	34

4.2.	Data Acquisition System design	35
4.3.	Linear Actuator assembly	37
4.3.1.	Structure	37
4.3.2.	Electronic Components	39
4.3.3.	Control	40
4.4.	Load Cell assembly	42
4.4.1.	Structure	43
4.4.2.	Electronic Components	43
4.4.3.	Control	44
5.	CALIBRATIONS	45
5.1.	Velocity characterization of the Linear Actuator	45
5.1.1.	Needle real feed velocity determination	45
5.1.2.	Linear Actuator feed	47
5.2.	Load Cell calibration	48
5.3.	Load Cell sensitivity	49
5.3.1.	Measurements Frequency	49
5.3.2.	Load sensibility	50
5.4.	Linear Actuator vibrations	52
5.4.1.	Vibration Analysis	54
5.4.2.	Testing results	55
5.5.	Needle Angle determinations	56
6.	METHODOLOGY	59
6.1.	Control Variables	59
6.2.	Materials	60
6.2.1.	Hypodermic needles	60
6.2.2.	Biological tissue	63
6.2.3.	Sample recipient	63
6.3.	Experimental procedure	63
6.3.1.	Machine setup and sensors calibration	63
6.3.2.	Tissue sample preparation	64
6.3.3.	Needle placing	66
6.3.4.	Test procedure	67
6.3.5.	Experiment wrapping procedure	68
7.	DATA ANALYSIS AND PRELIMINARY RESULTS	69
7.1.	Data acquisition and calculations	69
7.2.	Cutting and Friction forces	72

7.3.	Stiffness force	73
7.4.	Superficial Deformation	75
7.5.	Cutting force per Depth.....	75
7.6.	Friction per Unit of Contact Area	76
7.7.	Results.....	78
7.7.1.	Superficial Deformation	80
7.7.2.	Stiffness force	81
7.7.3.	Cutting forces.....	82
7.7.4.	Friction forces	83
8.	DISCUSSION AND CONCLUSIONS	85
8.1.	Discussion	85
8.2.	Conclusions.....	86
8.3.	Future Work.....	86
9.	REGULATIONS AND ENVIRONMENTAL STUDY	87
9.1.	Regulations applied	87
9.2.	Environmental study	88
10.	PROJECT BUDGET	91
10.1.	Manufacturing cost	91
10.2.	Personnel cost	92
10.3.	Experimental trials cost	94
10.4.	Total budget for manufacturing.....	95
10.5.	Total budget of the project	95
11.	BIBLIOGRAPHY	96

1. Preface

1.1. Project Origin

In early 2020, this project was presented to me by Professor Antonio Jose Sánchez Egea, from the Mechanical Engineering Department of the Universitat Politecnica de Catalunya. By that time, he already had an idea of the design he wanted to make, and from then, he involved me in every step of the project.

This paper aims to open a research topic on our University: the study of different needles' mechanical behaviors when pricking biological tissues. Including the characterization of different mechanical parameters, such as cutting and friction forces, feed rate, surface stress, etc. All of them are involved in the interaction between the needle and the soft tissue when an insertion is carried out.

1.2. Motivation

This project has been a great opportunity to collaborate on the process of creating a new device, by doing its design, manufacture, and conducting experimental tests to describe the functionality. I have also been able to use the created device to conduct its first needle tests.

Thanks to the experimental work done, I have learned different engineering disciplines, such as electronics, mechanics, and biomechanics. All these opportunities have been a great source of motivation while working on this project.

1.3. Requirements

For the realization of this project is needed to have some knowledge, about Arduino and its code, besides some skills in CAD design and electronics. Some basic knowledge is also needed in viscoelastic materials to understand the mechanics involved.

2. Scope

2.1. Project Objectives

The main objective of this project is to design, manufacture, and do experimental testing of a mechanical test bench to study the behavior of needles while being inserted in soft-tissues. This project aims to start a research area in our University about the study and characterization of different needles used in various medical procedures, to optimize these procedures and reduce the side effects.

The secondary objectives are the following ones:

- Collect information about previous research works and finding the main conditions for designing and manufacturing a mechanical bench to perform the picking experiments.
- Design the experimental tests with different hypodermic needles and feed velocities, to describe the cutting and frictional forces.
- Analyze the mechanical performance and describe the device's range capacity and accuracy in the data acquisition.
- Describe the influence of the operating parameters in the cutting and frictional forces and the needles' morphology.
- Recollect all the technical specifications of the prototype manufactured and its possible modifications.

2.2. Project Scope

This project first characterizes and manufactures a mechanical test bench according to the literature's requirements. It gathers some of the recent investigations and discoveries made in this research area. Part of this project focuses on explaining the design and assembly made, with all the technical specifications referred to the elaboration of technical drawings, the electronic circuits, and the electronics control. Some of the required calibration procedures of the machine's different elements include the explanation of its functionality and the possible modifications that could be made.

After defining this machine's limits, an experimental protocol is proposed to achieve the best data acquisition. Then, several conclusions are withdrawn regarding cutting forces and the test bench's operation. Finally, we also include the estimated budget and the environmental impact of this research work.

2.3. Chronogram

For this project, I was made a chronogram, to track the hours spent on each task. Although the project officially started in September, there had been inverted some hours in the summer months to familiarize and learn Arduino coding and electronics. This chronogram approximation helped with the realization of the project's economic study.

Activities	Months															
	Agust			September			October			November			December		January	
Arduino code learning	■	■	■	■	■											
Information serch				■	■	■										
Machine Final Assembly				■	■	■	■									
Thecnical Documentation				■	■	■	■	■	■							
Machine Calibrations							■	■	■							
Test Preparation								■	■	■						
Needle Experimentation									■	■						
Data Analysis										■	■	■	■			
Memory Writing										■	■	■	■	■	■	■

3. Introduction

Needles are one of the most used tools in medical procedures these days. They are non-invasive tools, used from the most routine procedures to complex operations. Despite its common and effective use, a great interest has grown in the needle's behavior while puncturing into a tissue, to minimize the impact on the patient and improve the performance of the needle.

The studies made on this topic, focus on analyzing and understanding the forces produced while inserting a needle into a tissue. These forces occur as a tissue response to the needle insertion, and it is thought that the reduction of these forces would directly impact the tissue tearing and puncture accuracy. By reducing the tearing, the tissues can recover faster from an insertion, though this may not be critical in blood tests, it is of particular importance in a cerebral insertion.

The insertion forces' have an impact on the needle's geometry, causing deflection on them and shifting its trajectory. [1] Estimating the trajectory when the needle is being inserted has particular importance in delicate operations such as biopsies, where tissue samples are extracted from the body. In the case of a biopsy, improving each puncture's accuracy can result in extracting the desired samples in good conditions for its analysis. This trajectory estimation also leads to making delicate procedures without affecting the nearest organs. For example, in the epidural anesthesia case, the puncture accuracy could reduce the risk of Dural Puncture. This happens when the needle or catheter punctures the dura and arachnoid maters, delivering prolonged headaches over time. [2]

3.1. Needle insertion mechanics

To understand what recent studies are focused on, it must be explained what happens while a biological tissue is being punctured. When the needle touches the surface of a tissue, several forces appear contrary to the insertion. These are produced by the surface tension of the tissue, and its viscoelastic properties. When the needle tip first interacts with the tissue surface, this starts deforming until the needle manages to exceed the elastic limit of the surface. Right after, the needle tip begins to penetrate onto the inner layers and the needle walls start inserting into the tissue. Figure 3.1 displays a real image of needle insertion for vaccination.



Figure 3.1 Vaccination insertion. [18]

Special emphasis is placed on the penetration of the first tissue layers since they are characteristic for having higher resistance to the needle's cutting effect. The overcome of the tissue's surface tension produces a characteristic peak of force called, Maximum Stiffness force. After this first penetration, the needle's tip continues to penetrate the inner layers of tissue, creating the cutting force. The cutting force is joined by the friction force, produced with the advance of the needle walls into the material. These two forces appear together during needle insertion and increase according to the incrementation of the needle area's inserted into the material. Figure 3.2 shows an outline of needle penetration and the forces involved in the process: stiffness force, cutting force, and friction force.

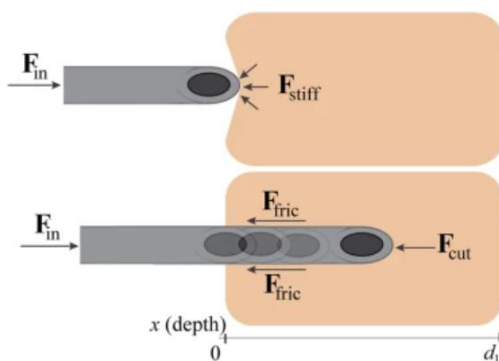


Figure 3.2 Needle insertion forces representation. [3]

The summary of needle insertion forces can be outlined as the following equation:

$$F_{in} = - F_{stiff} - (F_{cut} - F_{fricc}) \tag{Eq.1}$$

Other factors, besides the physiology and viscoelastic properties of the pricked tissue, influence the interaction mechanics between the tissues and the needles. These factors can be due to the needle design properties: needle gauge, manufacturing tolerances and diameters, as well as to different insertion process factors: insertion velocity, penetration angle or rotatory movement.

3.2. State of Art

The following paragraphs gather several studies of significant interest. They explain some influential parameters investigated, and discoveries made on the insertion forces and the needle insertion mechanics. After the exposure of these studies, some of the prototypes created to realize the experimental procedures are displayed for the understanding of the prototype requirements.

3.2.1. Effect of needle diameter and tip geometry

Okamura et al. 2004 [4] obtained an apparent increase in the cutting and friction forces related to the increase of diameter. This effect is easily explained, the incrementation of diameter leads to a larger needle surface inserted, and bigger cuts on the tissue, consequently it is appreciated an increase in the friction and cutting forces.

Webster et al. 2005 [5] conducted a series of experiments with different needle tip angles, going from 5° to 80°. Their study observed how the deflection effects on the needle increased as the needle tip angle decreased.

Misra et al. 2012 [6] observed the same force behavior as *Okamura* regarding the needle diameter in hydrogel samples. Their study included some observations on decreasing needle deflection in a 2 mm needle diameter than a 1mm one. It also reported how the angle of the needle tip influenced the penetration forces by testing 30° and 75° needle tip angles. It explained that the largest needle tip angle compressed more the tissue, and this compression was conducted on higher penetration forces, with a very slight increase of deflection caused by the tip's geometric asymmetry. For the smallest needle tip angle, the forces produced were smaller and the deflections too.

3.2.2. Insertion speed effects

Mahvash et al. 2010 [7] Initiated a study on tissue rupture based on the insertion speed of the needle. They developed a mathematical model to make predictions on the tissue rupture. In one of their observations, it was mentioned the relation between the reduction of the stiffness force due to the increase of speed, despite observing an increase in the energy release rate.

Jiang et al. 2014 [8] performed some tests with a 7G needle and an artificial tissue made of *Polyvinyl Alcohol, PVA*. For 0.5 mm/s to 20 mm/s insertion speeds, it was observed how the force per position curves augmented as the insertion speed increased, even though for greater velocities than 5 mm/s the penetration force appeared to be independent of this factor.

3.2.3. Other parameters

The study of the parameters described before resulted in further studies in other aspects that could be modified to reduce the insertion forces. These go from adding different relative movements during the insertion process to modifying needle geometry. The following paragraphs expose some of the investigations made.

3.2.3.1. Needle geometry modification

Aoyagi et al. 2012 [9] worked on the manufacture and testing of a needle that mimicked the micro-serrated geometry of mosquito maxilla. Intending to remove the stiffens produced on the cutting force, thanks to the micro saws' gripping effect when inserted in the tissue. Despite observing lower insertion forces while the needle was being inserted, the saws' anchoring effect increased the forces produced while extracting the needle, resulting in an average force similar to the one produced by a regular needle without a micro-saw. Figure 3.3 displays the micro-saws made on the needle.

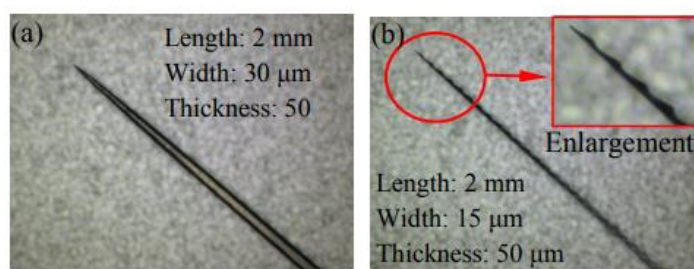


Figure 3.3 Optical images of the fabricated needles. [9]

3.2.3.2. Needle surface modification

Gao et al. 2020 [10] exposed a series of simulations and tests, where the surface of the needle was modified with a hydrophilic solution made of Polyvinylpyrrolidone, PVP and ketone. These components were selected because of their non-reactive nature with the needle material and because of its biocompatibility. The coating results were surprisingly positive, decreasing deformations were observed in the tissue because the coating lubrication and the friction forces were much lower than the frictional forces produced with a non-coated needle. It was clear that the effect of coating the needle reduced the stress produced in the tissue. Figure 3.4 displays the images of the coated and not coated surfaces of the needles.

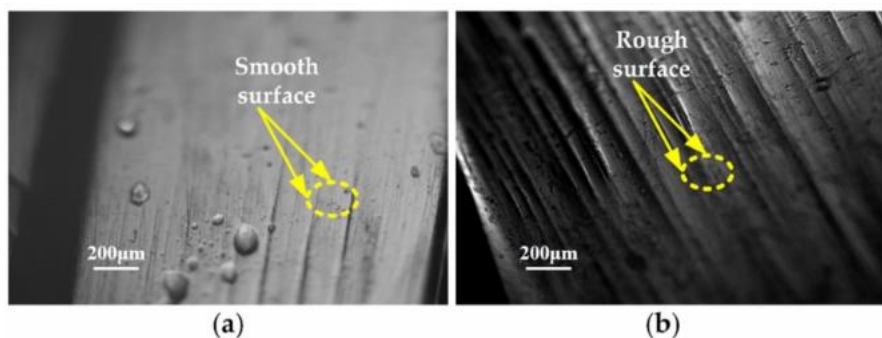


Figure 3.4 Microscopic view: a- coated needle and b- regular one. [10]

3.2.3.3. Needle tip geometry modification

Giovannini et al. 2017 [11] carried out a study on different Biopsy punches with micro-serrated tip geometries to study the behavior of the insertion forces. After the manufacturing and testing of the punches, they reduced insertion forces by 20-30% because of these micro saws at the tip. Figure 3.5 displays the 3D punch models.

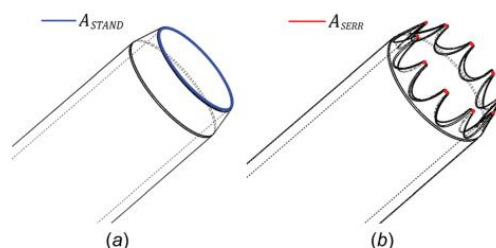


Figure 3.5 a- Normal punch, b-micro-serrated punch. [11]

Lehocky et al. 2017 [12] focused their study on the design and simulation of filled needles for robot-controlled brain insertions. These robot-controlled insertions followed curvilinear paths, which reduced the tissue damages produced by linear paths. The usual needle used in these procedures are blunt ones, as their geometry without sharp filets is safer. Lehocky's objective with the design made was to create a safe needle for brain insertions, preserving the bevel typed needles' asymmetry and steering behavior, to facilitate the curvilinear movement to the robot. However, they ended up concluding that the tissue cracks had much more influence on the steering. Figure 3.6 displays the design proposed.

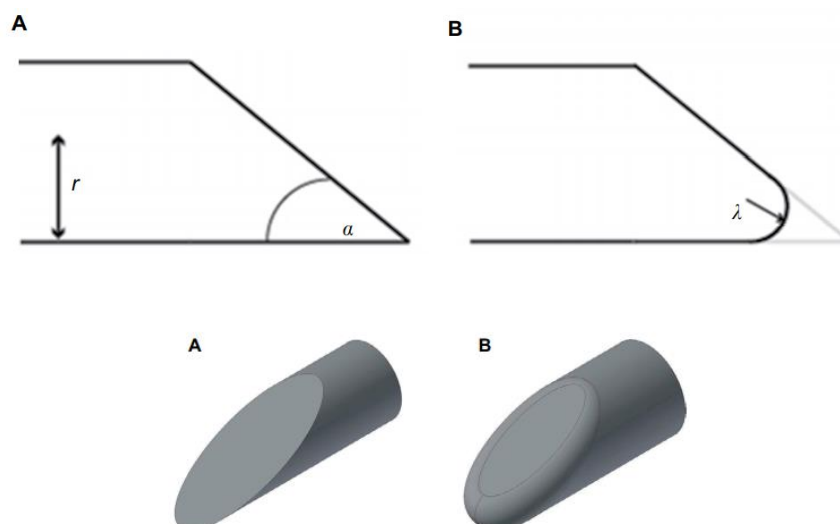


Figure 3.6 A- sharped bevel needle type, B- Filled bevel typed needle. [12]

3.2.3.4. Incorporation of an ultrasonic vibration movement

Begg et al. 2014 [13] conducted a study on the incorporation of extended audible vibration frequencies into the hypodermic needle insertion mechanism. They obtained very positive results for a range of axial vibration frequencies from 50 to 500Hz. It was seen a decrease in insertion forces, and consequently, reduced the damage produced on the tissue.

3.2.3.5. Including a relative rotational movement to the needle

Giovanini et al. 2018 [14] conducted a study that aimed to find the optimal insertion speeds for different needle geometries and procedures. They analyzed the impact of rotation on the needle, and after testing a 14G cannula to the same tissue with different rotational speeds, ranging from 0.5 to 6 mm/s. It was determined that the needle's rotational speed was crucial when the axial insertion speed was lower, between 0.5 and 2mm/s. Reductions of 50 to 35% of the axial penetration force were observed thanks to needle rotation.

3.2.4. Test benches created for the experiments

This subsection displays different mechanical test benches created for some of the experiments mentioned above. All of them have in common the need to provide an axial movement to the needle and a digital data recollection. Although it is seen how the design and tools used to accomplish these requirements are different for each prototype.

DiMaio et al. 2003 [14] created a test bench in which a high-speed camera recorded the needle position and the deformations created in the analyzed tissue. In this prototype, the needle moved axially thanks to two robotic arms that pushed the needle through the material tested. Figure 3.7 displays the prototype created.

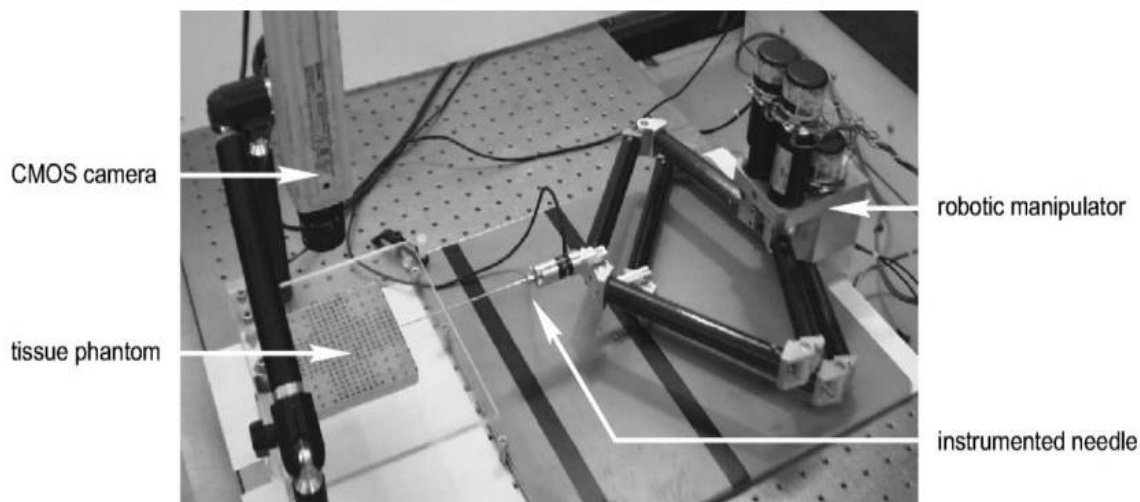


Figure 3.7 DiMaio et al. 2003 experimental setup. [14]

Jiang et al. 2014 [8] developed a test bench in which the function of providing an axial movement to the needle was provided with a linear actuator. For the recording of the forces produced in the process, they selected a mechanical torque sensor positioned on the needle shaft. Figure 3.8 displays the prototype created.

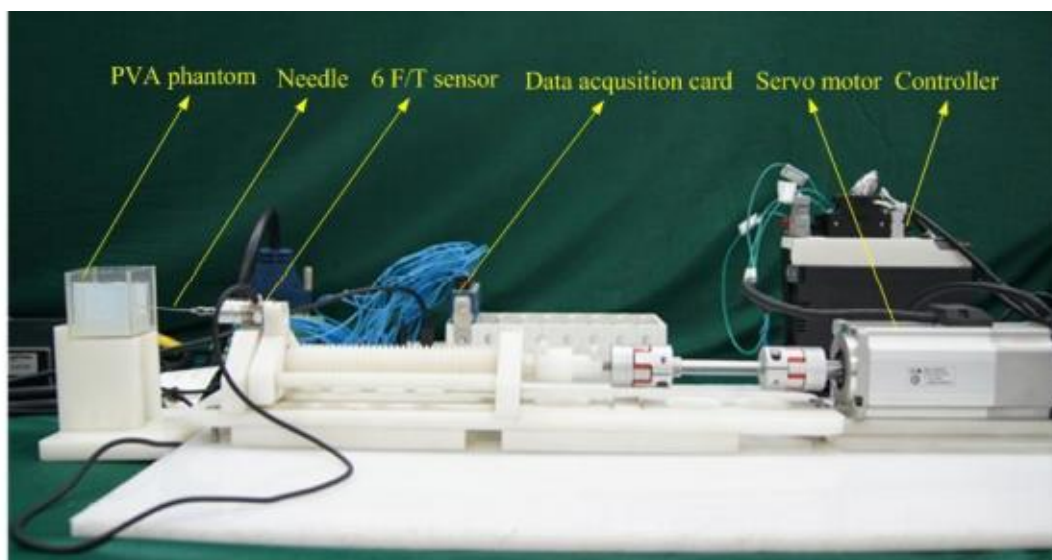


Figure 3.8 Jiang et al. 2014 experimental setup. [8]

Giovannini et al. 2018 [14] arranged their prototype like the previous one, with the usage of a linear actuator to provide the needle with an axial movement, but *Giovannini* added a second motor that not only was used to hold the needle also to give it a rotational movement. For data registering, they used a torque sensor and a dynamometer at the PVA sample base. Figure 3.9 displays the prototype created.

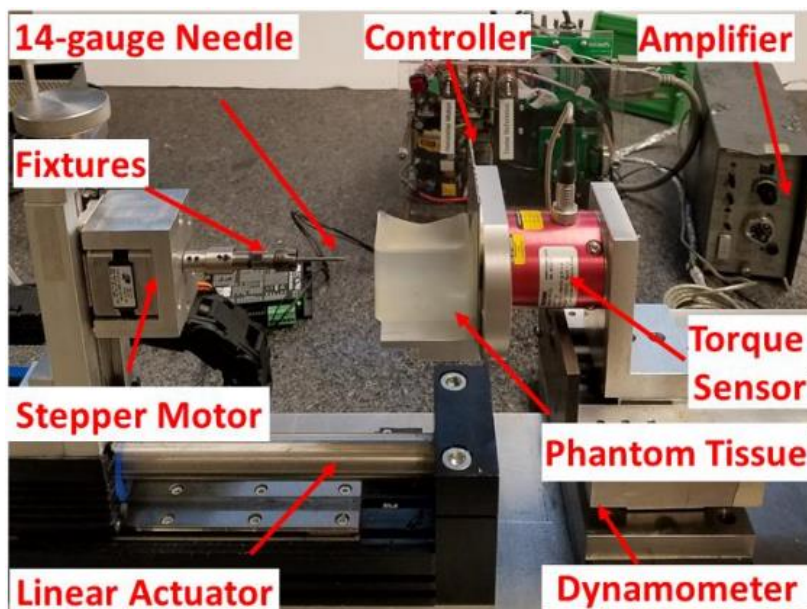


Figure 3.9 *Giovannini et al. 2018* experimental setup. [14]

Mahvash et al. 2010 [7] proposed a prototype similar to the previous ones, this prototype stands out for the vertical arrangement of the machine, producing an axial movement parallel with the gravity vector. Figure 3.10 displays the mentioned prototype.

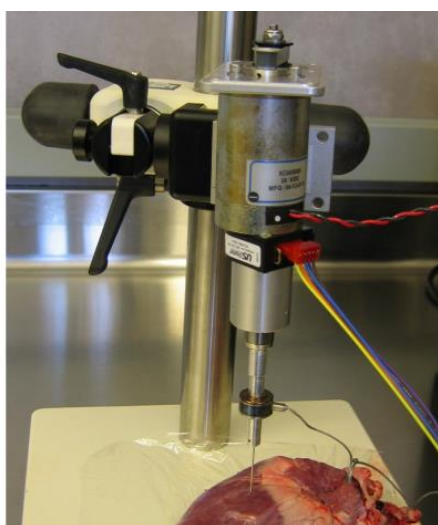


Figure 3.10 *Mahvash et al. 2010* experimental setup. [7]

3.3. Mathematical modelling of Insertion forces

Given the general behavior of the involved insertion forces and prototypes, this section of the chapter details the equations related to the different forces associated with needle insertion. *Jiang et al. 2014* [8] simulated and analyzed the three-needle insertion forces produced while pricking a tissue, concluding on this mathematical model:

3.3.1. Stiffness force

Starting with the $f_{\text{stiffness}}$, produced by the viscoelastic forces of the pricked material. The modelling used a contact model between the needle and the tissue is represented in Figure 3.11.

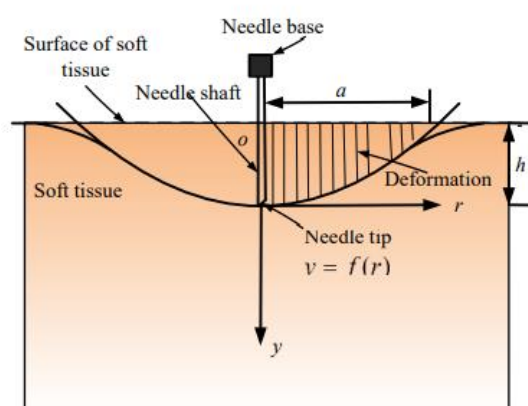


Figure 3.11 Contact modelization of the needle and tissue. [8]

This model has been solved with Henkel's transforms and the double derivatives theory, resulting in the following formulas:

$$h = \int_0^1 \frac{f'(x)}{\sqrt{1-x^2}} dx \quad (\text{Eq.2})$$

$$f_{\text{stiffness}} = 2E_r a \int_0^1 \frac{x^2 f'(x)}{\sqrt{1-x^2}} dx \quad (\text{Eq.3})$$

The function $f(x)$ refers to the deformation curve, being the needle tip, the beginning of the curve. Then: $y = f(r)$ where $r = ax (r \leq a)$ so that $f(0) = 0$. Being h the depth penetrated by the needle, and a the radius of the needle contact circle.

E_r is the reduced Young Module that was determined as it follows:

$$\frac{1}{E_r} = \frac{1 - \nu_1^2}{E_1} + \frac{1 - \nu_2^2}{E_2} \quad (\text{Eq.4})$$

Being E_1, E_2, ν_1, ν_2 the respective Young's modulus and Poisson's ratio of the needle and the tissue.

Even though the stiffness force approximation is proper (Eq.3), almost all needles have a sloping tip. This lead to redefine the formula of the deformation to $f(x) = \varepsilon x$ being $\varepsilon = a \cot \alpha$ with a penetration angle of 90° , and assuming a tip bevel angle of $\alpha = 15^\circ$, resulting in the following formula

$$f(x) = ax \cot \alpha \quad (\text{Eq.5})$$

Incorporating this new formula into (Eq.2) and (Eq.3) $f_{\text{stiffness}}$ is redefined as:

$$f_{\text{stiffness}} = \frac{2}{\pi} E_r \tan(\alpha) h^2 \quad (\text{Eq.6})$$

Including this equation to the previous one (Eq.6) the definition of the Reduced Elastic Module (Eq.4), can be reduced as it follows:

$$\begin{aligned} f_{\text{stiffness}} &= \frac{2E_1E_2}{\pi[E_2(1 - \nu_1^2) + E_1(1 - \nu_2^2)]} h \cdot \tan(\alpha) \cdot h \quad (\text{Eq.7}) \\ &= \frac{2E_1E_2}{\pi[E_2(1 - \nu_1^2) + E_1(1 - \nu_2^2)]} l \cdot h \end{aligned}$$

$$f_{\text{stiffness}(i)} = \frac{2}{\pi} \psi(E_1, E_2, \nu_1, \nu_2) l_i \cdot h_i \quad ((0 < h_i \leq z_i, 0 < l_i \leq d_i) i = 1,2,3,4,5) \quad (\text{Eq.8})$$

Where h y l represent the respective axial and transverse lengths of the inserted needle, and d_i, z_i are the insertion diameter of the needle, representing the maximum l of the needle and the maximum length of the needle bevel. To find $f_{\text{stiffness max}}$ it is only needed to replace in the formula h and l for d_i y z_i . See the representation of these parameters in the following Figure 3.12.

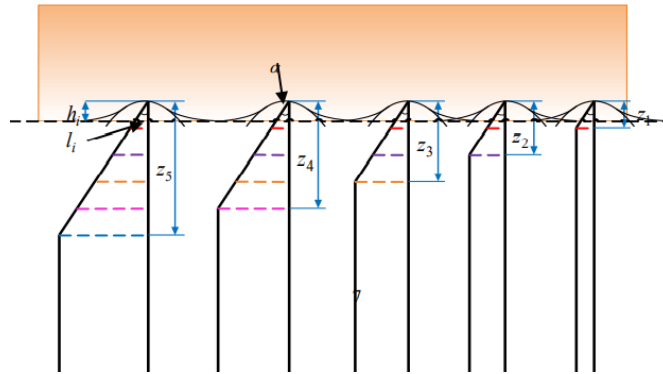


Figure 3.12 Different needle penetrations. [8]

3.3.2. Friction force

Jiang proceeds to explain how the f_{friction} was modeled from the following equation:

$$f_{\text{friction}} = \mu F_n \quad (\text{Eq.9})$$

Being F_n normal force contrary to movement due to tissue deformation. It is explained how different studies have observed that the force distribution between the needle and tissue is approximately uniform along the shaft. That is why it is decided to model the Normal Force with a linear stiffness coefficient, following *Winkler's foundation* [16], see Figure 3.13.

$$F_n = kh\Delta \quad (\text{Eq.10})$$

Where Δ is the settling amount, k the foundation modulus and h the needle contact length.

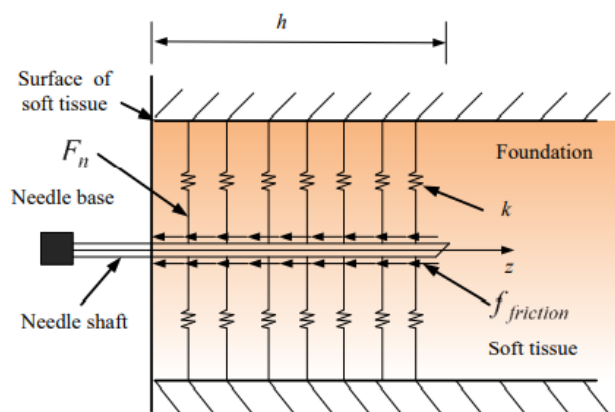


Figure 3.13 Modified Winkler's foundation model for friction force. [8]

For the foundation modulus, it was selected the one developed by *Biot (1937)* [17] of an elastic beam:

$$k = \frac{\beta E}{(1 - \nu_2^2)} \left[\frac{E_2 b^4}{E_1 I (1 - \nu_2^2)} \right]^\gamma \quad (\text{Eq.11})$$

In this case, the working conditions selected were $\beta = 0,65$ y $\gamma = \frac{1}{12}$ leading to the following expression:

$$k = \frac{0.65 E_2}{1 - \nu_2^2} \sqrt[12]{\frac{E_2 b^4}{E_1 I (1 - \nu_2^2)}} \quad (\text{Eq.12})$$

Once it was incorporated (Eq.12) to the frictional force equation (Eq.3), it is simplified the equation using $\Delta = D/2$ y $b = \pi D$, being D the outer diameter of the needle:

$$f_{\text{friction}} = -\frac{\mu D}{2} \frac{0.65 E_2}{1 - \nu_2^2} \sqrt[12]{\frac{E_2 (\pi D)^4}{E_1 I (1 - \nu_2^2)}} h \quad (\text{Eq.13})$$

3.3.3. Cutting force

I was finally proceeded to mention that the f_{cutting} is constant:

$$f_{\text{cutting}} = C \quad (\text{Eq.14})$$

In the following equation are gathered *Jiang's* mathematical modulations for all the forces produced on the needle insertion process and its removal:

$$\left\{ \begin{array}{ll} f_{\text{stiffness}} = \frac{2}{\pi} E_r \tan(\alpha) z^2 & z_A \leq z \leq z_B \\ f_{\text{friction}} + f_{\text{cutting}} = -\frac{\mu D}{2} \frac{0.65 E_2}{1 - \nu_2^2} \sqrt[12]{\frac{E_2 (\pi D)^4}{E_1 I (1 - \nu_2^2)}} z + C & z_B \leq z \leq z_C \\ f_{\text{friction}} = -\frac{\mu D}{2} \frac{0.65 E_2}{1 - \nu_2^2} \sqrt[12]{\frac{E_2 (\pi D)^4}{E_1 I (1 - \nu_2^2)}} z & z_C \leq z \leq z_D \end{array} \right. \quad (\text{Eq.15})$$

Where z_A is the position of the tissue before being penetrated, z_B the point at where the needle overcomes the surface tension of the tissue and begins to penetrate, z_C the point where the needle insertion movement is stopped and the extraction movement start, and finally, z_D the position where the tissue and needle are no longer in contact.

3.4. Soft-Tissue Viscoelasticity

This section exposes an overview of the complex mechanical properties of biological tissues, as their behavior significantly influences the forces that appeared in the insertion forces.

In the article "*Tissue mechanics regulate brain development, homeostasis and disease*" [19], it is explained how many mechanical properties are defined by the fibers' proprieties conforming to the soft tissues. They give an example of the human brain's extracellular matrix, ECM: a network of extracellular macromolecules that provide structural and biochemical support to surrounding cells. This occupies 20% of the brain and it is composed mainly of glycosaminoglycans, including hyaluronic acid and proteoglycans. The non-fibrillar nature of its components contributes to the low elastic modulus of the brain.

On the contrary, most soft tissues are structurally supported by a network of fibrous proteins, such as fibrillar collagens, which bring better elastic properties than the brain ones. Figure 3.14, shows the approximate young module of different tissues and organs that make up our body.

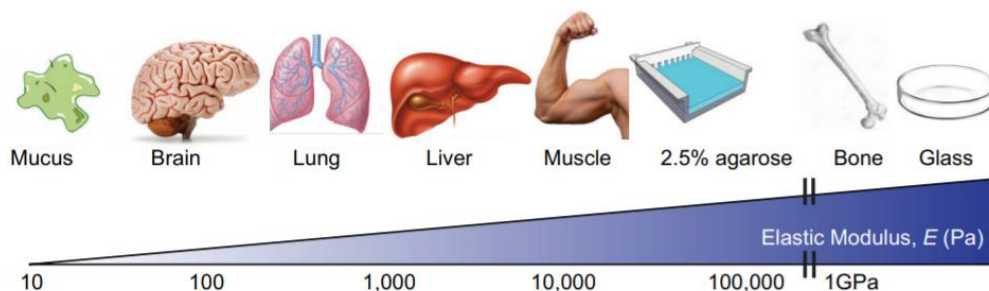


Figure 3.14 Mechanical properties of tissues. [19]

Regarding the soft-tissues tested in this project, soft tissues characterize for connecting, surrounding and giving support to internal organs and bones. Including muscle, tendons, ligaments, fat, fibrous tissue, skin, etc. The extracellular matrix ECM of soft tissues is partially composed of collagen and elastin. Fibroblasts are the typical cells that conform the tissue. The composing collagen of the ECM provides the tissue its characteristic stiffness, as the collagen fibers are inextensible, although they are somehow loose and wavy. See the collage fibers displayed in Figure 3.15. When the tissue deforms the collagen, fibers stretch and produce a growth in the tissue's stiffness force. See an example of a stress-strain curve in Figure 3.15.

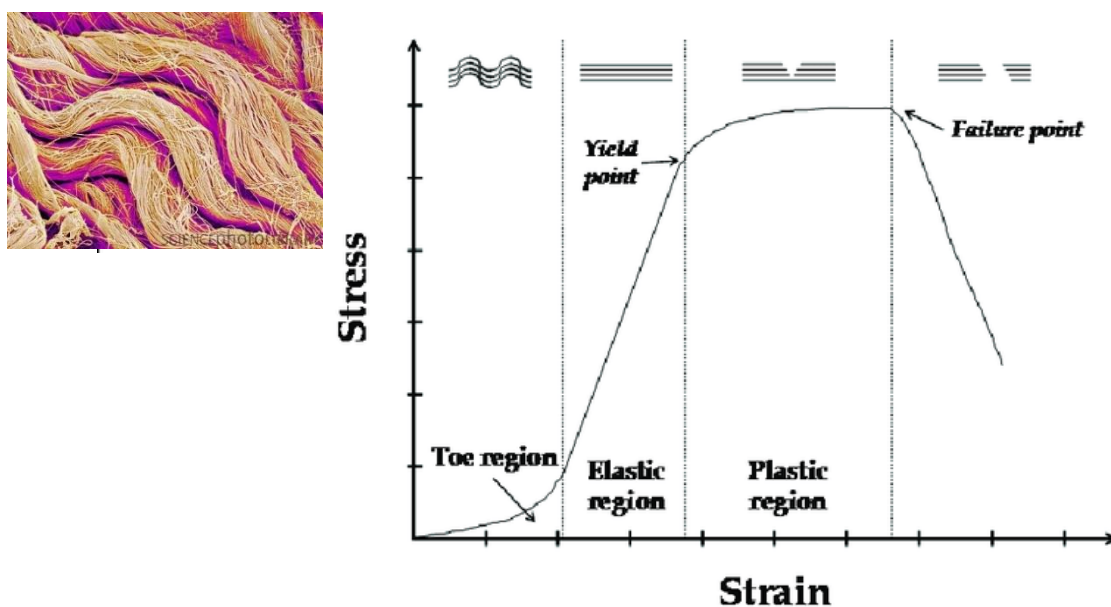


Figure 3.15 Collagen fibers, and stress-strain curve for destructive tensile testing of skeletal soft tissues. [20]

Soft tissues are hyperplastic materials with a nonlinear stress-strain curve and viscoelastic, incompressible, and anisotropic behavior, often modified by the stress of the tissue. [21] Viscoelastic properties observed in these tissues are explained in next paragraphs.

3.4.1. Relaxation

The relaxation refers to the return of the perturbed tissue into equilibrium. Contained in the elastic region of the stress-strain curve. See the stress-time behaviour schematics in Figure 3.16.

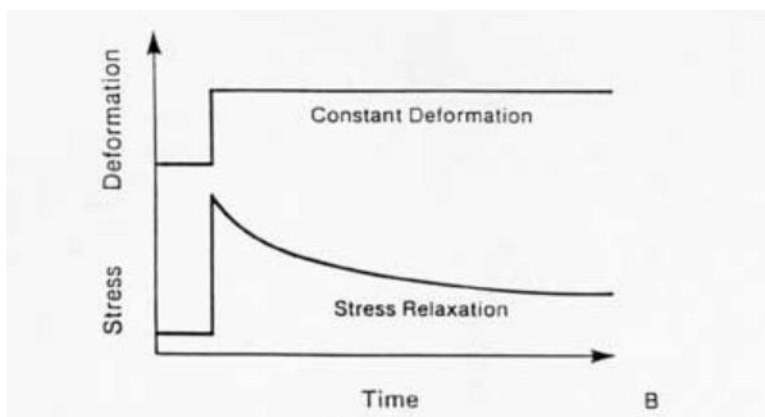


Figure 3.16 stress-time curve schematics for the understanding of viscoelastic behavior. [22]

3.4.2. Creep

Creep is the tendency of the tissue to move slowly and deform permanently due to mechanical stress. It is contained in the plastic region of the stress-strain curve. See the deformation-time behaviour schematics in Figure 3.17.

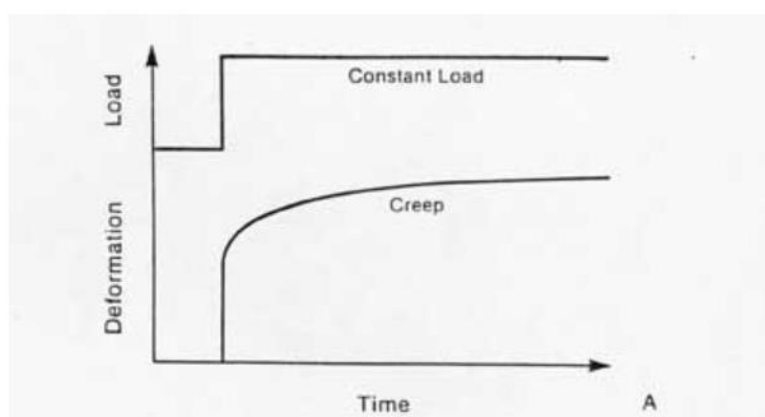


Figure 3.17 deformation-time curve schematics for the understanding of viscoelastic behavior [22]

The following Figure 3.18 displays the elastic recovery and creep's recovery for unloading:

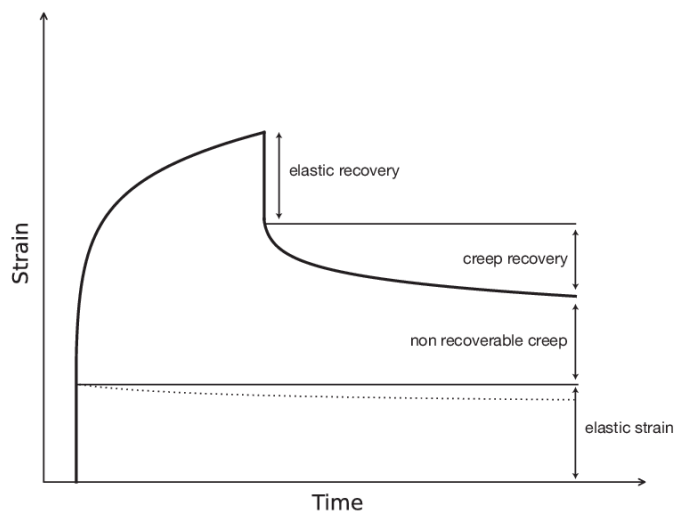


Figure 3.18 strain-time curve schematics for the understanding of creep recovery and viscoelastic behavior. [20]

3.4.3. Hysteresis

Hysteresis, is the dependence of the tissue state on its history, making the loading curve of the material does not match the unloading one. The strain energy lost between loading and unloading results is due to the internal friction and heat loss. See the stress-strain curve on Figure 3.19.

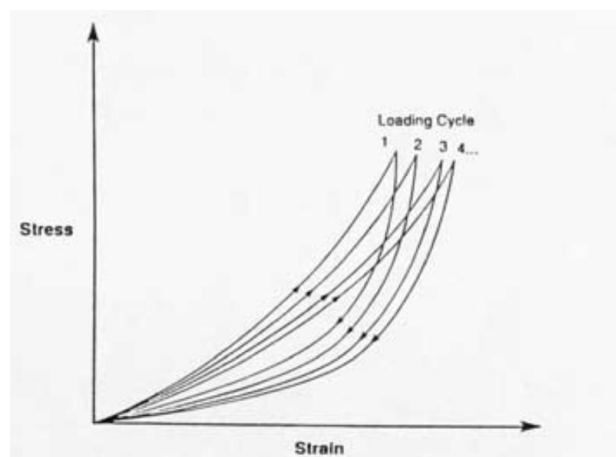


Figure 3.19 strain-stress loading cycle schematics for the understanding of viscoelastic behavior. [22]

As the *Orthopedic Bioengineering Research Laboratory at Colorado State University* web page says, the characterization of biological tissues' mechanical properties is not easy due to its nonlinear viscoelastic behavior. It continues to explain that recent mechanical studies made for it cannot predict general behaviors in tissues using different load conditions than those used in the model to

obtain the behavior coefficients. [23] Some studies on the mechanics of needle insertion have been made with Polyvinyl Alcohol, PVA and Polyvinyl chloride, PVC phantoms, created to mimic soft tissues' mechanical properties. Several studies focused on approximating PVC solutions to recreate the mechanical properties of different organs for academic purposes. [24]

3.5. Mechanical bench requirements and Test design

As seen in this chapter, the needle testings' machine requirements are, providing a linear movement to the needle and having some sensors to detect the tissue's changes by the needle insertion. Due to the current technology, this research area has extended to a point where the prototypes created add various relative movements to the needle. It is decided that future tests will contemplate the addition of these plugins in the prototype created. Thus, the machine's design must contemplate this option so that the prototype is somehow versatile.

The tests carried out in this project will focus on the characterization of different geometric hypodermic needle parameters, regarding the needle's diameter and bevel tip type, and their influence on the puncture's insertion velocities. Consequently, besides developing an in-house specific testing machine, the test's methodology and data treatment for this type of experiment on the prototype, will be created and detailed, to make a proper analysis of the forces involved. All these tasks are described in the different chapters of this project.

4. Design and Assembly

The mechanical bench was divided into two different parts, the first one englobed the machine driving part, and the second one focused on the data acquisition. Although both were complementary, it was decided to make them work independently since their functionalities were different and dividing them made both the electrical design process and the assembly of the prototype more agile.

4.1. Driving Part design

The driving part needed to provide a linear movement to the needle to simulate the insertion process. For this purpose, it was thought of as a linear actuator typically used in 3d printers. This component provided the linear movement of the needle and offered some versatility because of the multiple gadgets that could be attached to its moving plate. The needle attached to the moving plate with a stepper motor, subjected by a prefabricated motor holder, and a designed adapter inserted in the motor shaft, converting its diameter to the proper one where the needle was adjusted. Figure 3.1 shows the CAD design for this system.

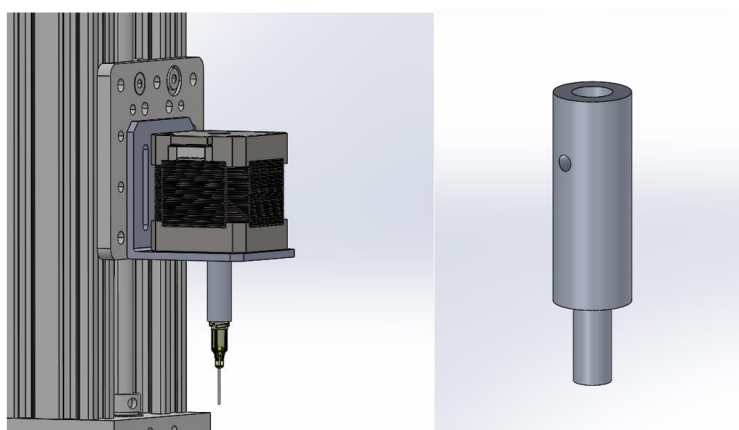


Figure 4.1 Needle holder attached to the linear actuator and needle adapter. [Own Source]

It was decided that the linear actuator should be placed perpendicular from the floor, positioning the axial needle axis parallel to the gravity vector. This decision was made because it was much easier to extract the forces produced if the needle movement followed the gravity vector. It was also designed a base to hold its weight and hold the electronics box positioning the linear actuator perpendicular to the floor. Figure 4.2 shows the inverted T-shaped structure and needle arrangement.

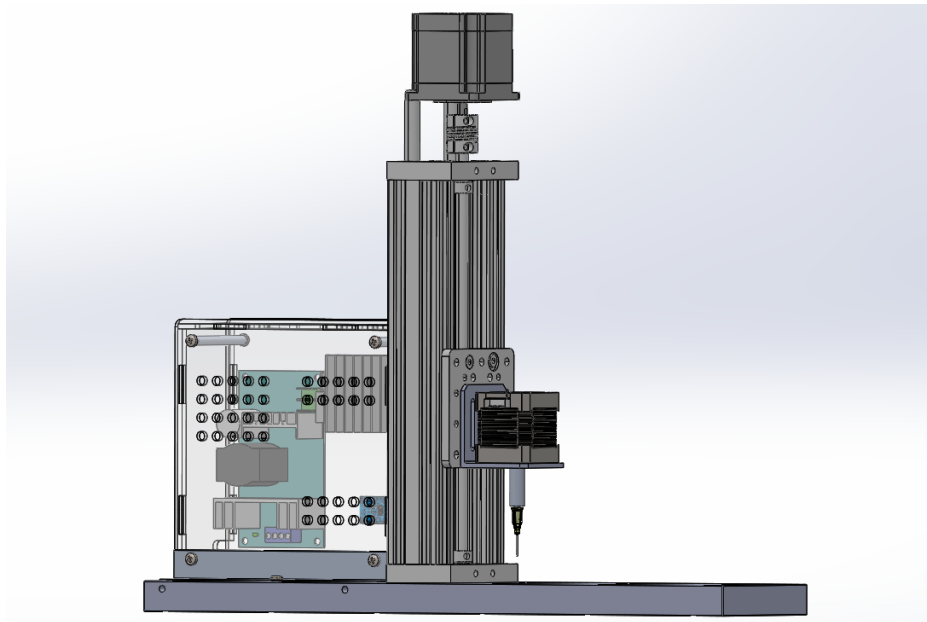


Figure 4.2 Linear actuator CAD assembly [Own Source]

4.2. Data Acquisition System design

This second part of the mechanical bench focused on the force measuring system. A load cell sensor was selected to record the forces produced. It was chosen a 1kg load cell so that the system could have high sensitivity in the records. For the correct placement of the load cell in the linear actuator base, it was designed a custom frame, and some supports to facilitate the positioning of the samples tested in it. Figure 4.3 shows the load cell and its frame, as well as the electronic to gather the signal data.

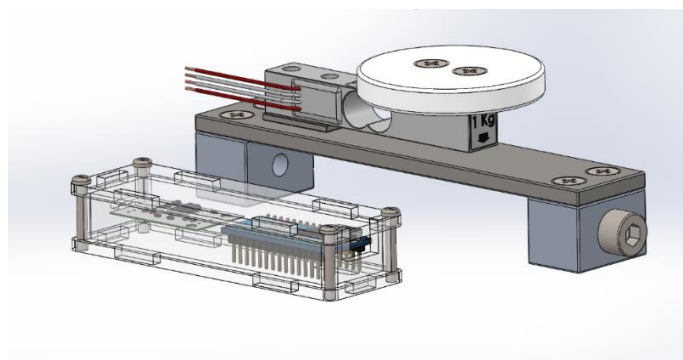


Figure 4.3 CAD model of the Force measuring system. [Own Source]

All components were controlled with Arduino controllers and a specific code designed for each system's functionalities. The following paragraphs explain these two parts of the mechanical bench, including the electronics design and the coding. Figure 4.4 and Figure 4.5 show the testing mechanical bench CAD design and the final manufactured prototype.

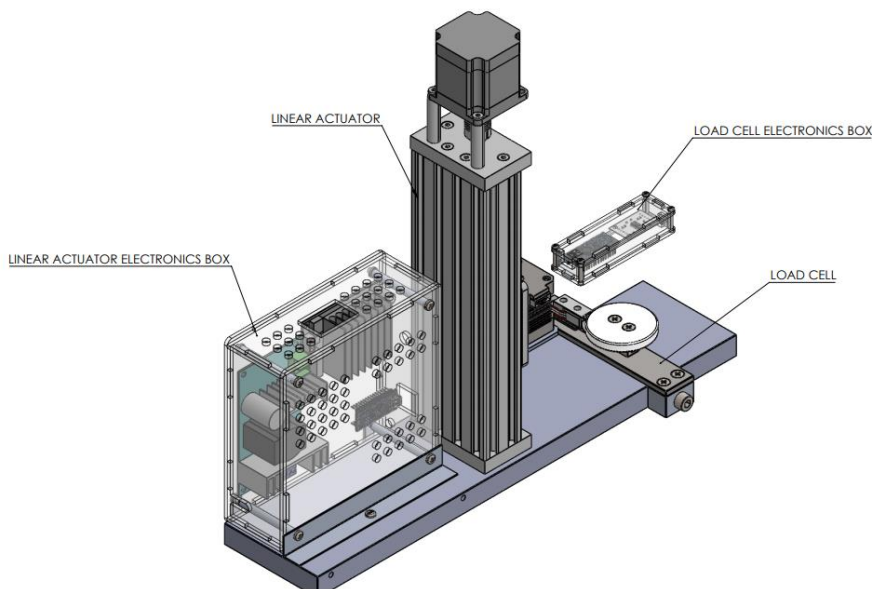


Figure 4.4 Machine CAD assembly. [Own Source]

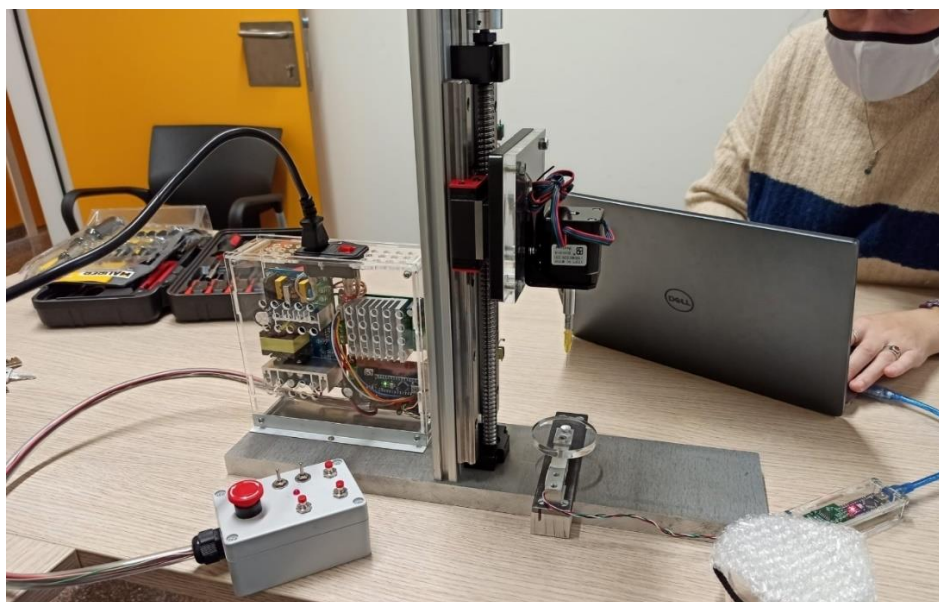


Figure 4.5 Manufactured mechanical test bench. [Own Source]

4.3. Linear Actuator assembly

This part of the machine englobes the mechanism that gives the axial movement to the needle, specifically its structure and control. The design was not only focused on incorporating an axial movement to the needle, but also on the versatility that it could have, depending on the type of experiment performed, and the possible relative movements introduced to the needle: translation, rotation, vibratory, or a combination of the previous ones. Figure 4.6 shows the inverted T-shaped structure.



Figure 4.6 inverted T-shaped linear actuator structure.

4.3.1. Structure

The linear actuator was the main structural component of the system, from the fabricant *HANPOSE*. This had incorporated a Nema 23 stepper motor of 2 phases and $1,8^\circ$ step-angle that provided the needle's axial movement. On to the moving plate of the linear actuator, it was mounted a Nema 17 stepper motor, which held the needle. This second motor also had a $1,8^\circ$ step angle and provided a second rotational movement to the needle while keeping the needle parallel with the gravity vector. All component datasheets are gathered in Annex A5. Figure 4.7 shows the motors mentioned before.

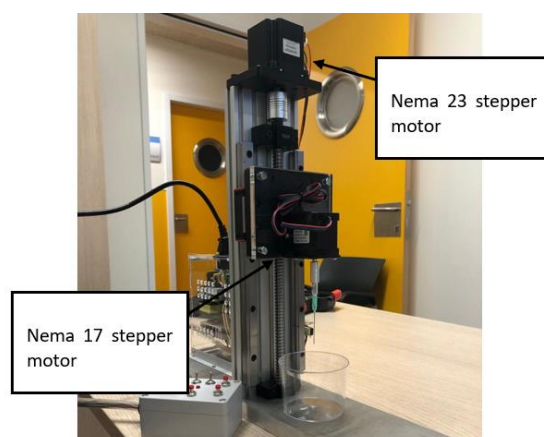


Figure 4.7 Linear actuator. [Own Source]

To attach the needles to the Nema 17 motor shaft an aluminum adapter was created to make motor shaft fitted into the extreme of a medical syringe. In this way, any needle-type could be easily placed and removed from the motor shaft. The positioning of the motor and the needle adapter's fabrication was critical as to the parallelism and perpendicular tolerances within the load cell and linear actuator structure. The adapter drawing is found in Annex A6. Figure 4.8 shows the Nema 17 motor and the aluminum adapter and the extreme of a syringe to act as a universal connector with the hypodermic needles.



Figure 4.8 Stepper with the universal needle adapter. [Own Source]

Screws attached the linear actuator to a 7075 T6 Aluminum base, designed and manufactured to ensure the perpendicularity of the linear actuator and consequently the needle with the ground. The load cell frame was fitted and adjusted into the base with screws. The load cell had to be centered concerning the tip of the needle, as the sensor recorded deformations and any eccentricity, which would modify the results. The design of the linear actuator base took into

consideration the geometric tolerances needed for this, see drawing in Annex A6. The frame was moved along the base, depending on the characteristics of the samples and needles tested. Figure 4.9 shows the linear actuator base with the load cell frame.

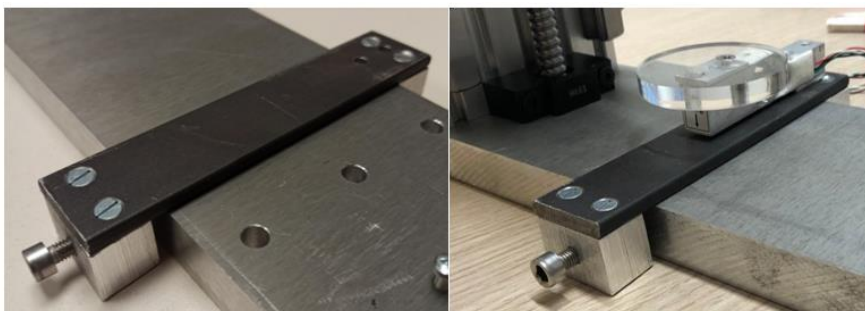


Figure 4.9 Load cell and its frame placed on top of the base. [Own Source]

All electronic components were arranged inside a methacrylate box that protected the most delicate ones such as the breadboard and prevented the wired terminals from producing electric shocks. The box was strategically perforated to ensure correct ventilation of the electronics and provide the exits of the multiple cables. It was positioned at the back of the test bench to avoid any interference with the tests. See drawings on Annex A6.

4.3.2. Electronic Components

The linear actuator's principal electronic components were both motors, the Arduino Nano, and the stepper motor driver. They were energized with a 24V / 6A power supply, connected to a general power button and a power plug. All datasheets are gathered in Annex A5. Figure 4.10 displays the arrangement of these elements in the methacrylate box.

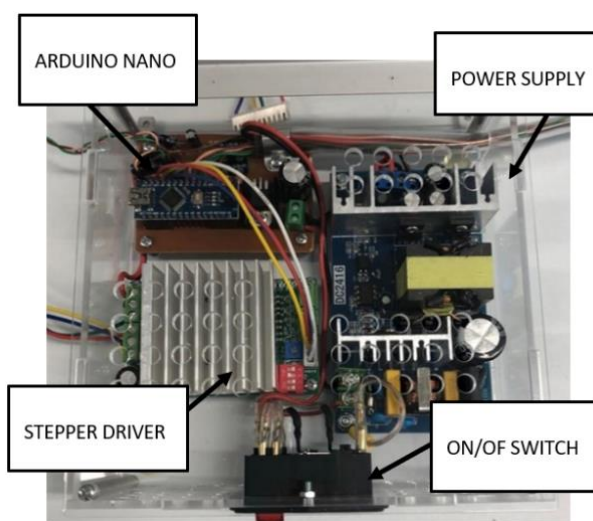


Figure 4.10 Main electronic components of the electronics box [Own Source]

The setup for the control and actuation of the axial motor, Nema 23, gathered some limit switches placed on the linear actuator's axial axis. These switches communicated with the Arduino nano and the stepper driver for emergency stops of the movement, adding a plus of safety to the system and preventing the load cell from breaking, see the datasheet on Annex A5. Also, it was created a customized button box connected to the Arduino nano controller to control the motor's velocities and the direction of the movement. The assembly of this part was designed and manufactured a breadboard that joined all components with Arduino Nano. The electric schematics of the components can be found in Annex A3. Figure 4.11 shows the limit switches mounted and the button box created for the project.

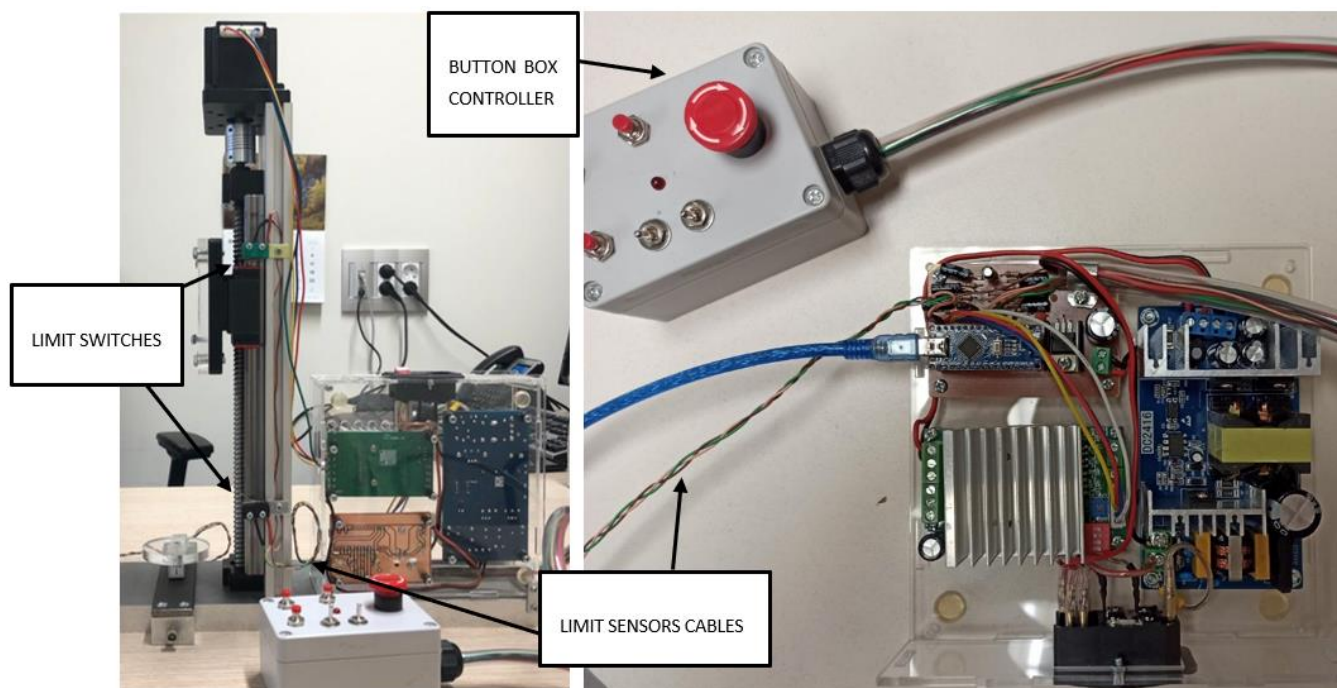


Figure 4.11 Linear actuator controlled by the bottom controller and delimited by the top and bottom end-switches. [Own Source]

4.3.3. Control

4.3.3.1. Linear Movement Control

The button box displayed in the previous figure controlled the linear actuator axial motor movement, it was equipped with 2 switches that allowed programming 4 different axial velocities on the code for this system. There were 2 other buttons, which defined the direction of the movement, and another one that will serve as an automatic mode in the future. It also included an

emergency stop button. The electric schemes of the button box and linear actuator code are found included in Annex A3, A4. See the button schematics of the button box in the following Figure 4.12.

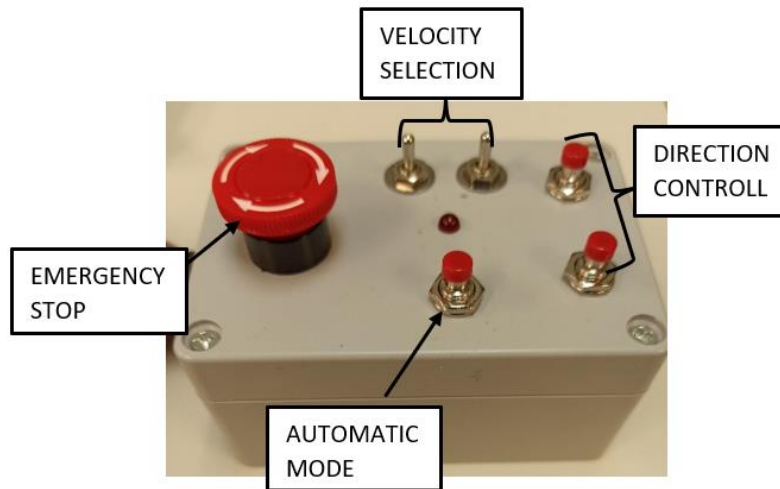


Figure 4.12 Button box schematics. [Own Source]

The system was programmed to stop any time the moving plate interfered with the limit switches placed on the linear actuator, see the sequence in Figure 4.13.



Figure 4.13 Moving plate interfering with the limit switch and consequently stopping the movement. [Own Source]

The velocities programmed in the linear actuator code were a combination of the button box switches, representing a binary matrix, 0 was equivalent to an off switch and 1 to a turned on one.

$$\begin{pmatrix} 00 & 01 \\ 01 & 11 \end{pmatrix} = \begin{pmatrix} V_1 & V_2 \\ V_3 & V_4 \end{pmatrix} = \begin{pmatrix} 800_{pps} & 600_{pps} \\ 400_{pps} & 200_{pps} \end{pmatrix} = \begin{pmatrix} 15,5_{mm/s} & 11,6_{mm/s} \\ 7,8_{mm/s} & 3,95_{mm/s} \end{pmatrix} \quad (Eq.16)$$

The motor's spindle speeds went from 100 rpm to 800 rpm, with 200 rpm incrementation of speed for each velocity programmed. For each spindle speed, it was found, the feed velocity of the needle

and the load cell leadscrew feed, turning out to be 3.95 mm/rev. In the following chapters are explained to more extent the calibrations made for this part of the mechanical bench.

4.3.3.2. Rotational Movement Control

For the control of the second motor, it was developed an android application prototype with the web page *Mit app inventor* [25]. This controlled the Nema 17 stepper motor with a Bluetooth module and an Easy Driver module. The layout created and the codes used enabled the velocity control, without the need to pre-program the velocities. Further works and investigations on a rotational needle movement could incorporate this control system to avoid making new button boxes for its control. In Annex A3, A2 can be found the electronics layout pictures and MIT app inventor and Arduino codes.

4.4. Load Cell assembly

The load cell sensor was attached to a frame designed to join the base of the machine. A screw regulated this frame to make the center of the load cell coincident with the position of the needle and avoid or minimize non-axial forces. The load cell was controlled by an Arduino Nano and the HX711 transmitter, both were held in a designed methacrylate box. Figure 4.14 shows the assembly of the force-measuring module.



Figure 4.14 Force measuring module. [own source]

The maximum capacity of this load cell was 1 kg. It was selected a load cell with this capacity to detect minimum changes in the forces produced. In the calibrations chapter, it is seen that this component was able to appreciate until 5 grams. See datasheet on Annex A5.

4.4.1. Structure

The load cell frame was designed to fit in the base support of the machine. It was composed of different aluminum and steel parts, which were scrap materials from the warehouse. Those parts needed to have parallel surfaces, to ensure that the load cell position was fully horizontal, and it did not disrupt the geometric experiment conditions. All the geometric tolerances are reported on the technical drawings, Annex A6.

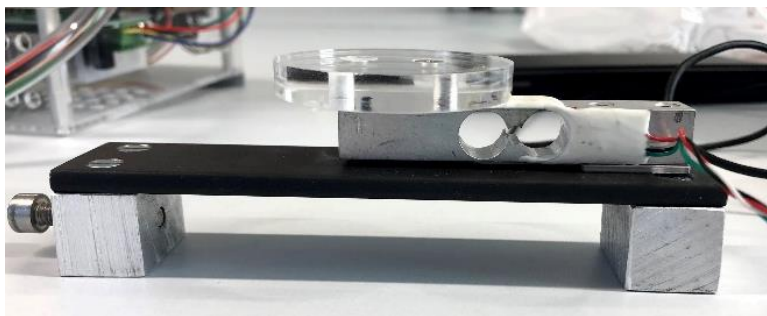


Figure 4.15 Frame of the load cell that is attached in support of the machine. [own source]

Above the load cell, it was placed a custom Methacrylate plate that holds the samples. Its design and manufacture also had to keep the parallelism tolerances in its surfaces, see drawings on Annex A6. Between the cell, the frame, and the plate, two pieces were placed. These pieces worked as spacers to leave the middle part of the load cell for an adequate recording. A methacrylate box was designed and built to keep all the electronic parts in a safe place.

4.4.2. Electronic Components

The electronic components involved in this system besides the load cell sensor were an Arduino Nano and an HX711 transmitter. This transmitter transformed the load cell analog signal onto a digital 24-bit sign. These two were welded to a breadboard that was modeled for this project. The electrical schemes of this system can be found in Annex A3.

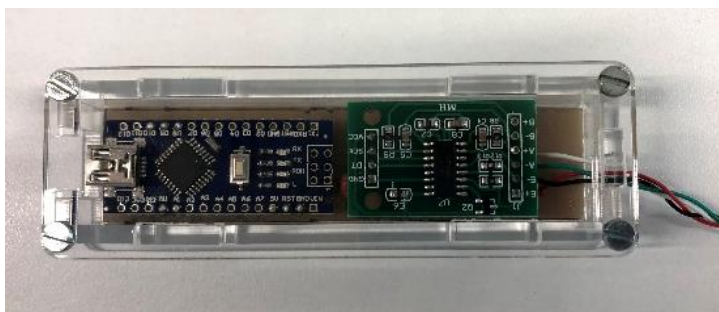


Figure 4.16 Arduino nano and its methacrylate box. [Own source]

4.4.3. Control

As mentioned before, the load cell registers were analog signals of the deformations happening in its forming material while weight was applied. Therefore, in future chapters, the conversion scale between these deformations produced and weight measurements is found. This scale was present in all force registration codes made.

For the needle force registers, an Arduino code was custom made to register the weight applied. It also displayed the relative time of the measurements within the start. This code had a registered frequency of 0.1s and made an auto-calibration on the beginning of the initial weight placed in the methacrylate plate. The Force Measuring code is displayed Annex A4.

5. Calibrations

5.1. Velocity characterization of the Linear Actuator

5.1.1. Needle real feed velocity determination

After defining the motor spindle speed, it was necessary to find the needle's translational velocity, the feed velocity of the needle, parallel to the linear actuator. This analysis was needed because the stepper movement, was transmitted to the needle support by a leadscrew. As shown in the following Figure 5.1, which screw pitch was not specified in the datasheet on Annex A4.



Figure 5.1 Linear actuator leadscrew and its needle support. [Own Source]

Some tests were conducted recording the time needed by the needle support, to go all over a certain distance and find the velocity it was moving. First, the limit switches were placed in the linear actuator, and the distance between them was measured, turning out to be 9.1mm. After that, with a chronometer, the time spent by needle support was measured to go through the distance between the limit switches. Four velocities were configured as a binary matrix code, shown below:

$$\begin{pmatrix} 00 & 01 \\ 01 & 11 \end{pmatrix} = \begin{pmatrix} V_1 & V_2 \\ V_3 & V_4 \end{pmatrix} = \begin{pmatrix} 800_{pps} & 600_{pps} \\ 400_{pps} & 200_{pps} \end{pmatrix} \quad (Eq.17)$$

Table 5.1 gathers a list of three measurements, and their average time for the different velocities used to travel 98.1 mm.

Table 5.1 Average time to travel 98.1mm when using different velocities. [Own Source]

	Time 1 (s)	Time 2 (s)	Time 3 (s)	Time 4 (s)
	6.42	8.35	12.49	24.7
	6.32	8.51	12.46	24.94
	6.36	8.57	12.78	24.87
	6.21	8.29	-	-
Average	6.327	8.43	12.576	24.836

It was found an approximate feed velocity for each programmed velocity by using the following equation:

$$V_{real} = \frac{Distance}{Average\ time} \rightarrow V_{1real} \frac{98.1mm}{6.33\ s} = 15.5 \frac{mm}{s} \quad (Eq.18)$$

After estimating the averaged velocities, it was approximated the margin error for each configuration, Annex A1.

$$V_{1real} = 15.5 \begin{matrix} +0.223 \\ -0.293 \end{matrix} mm/s \quad (Eq.19)$$

$$V_{2real} = 11.6 \begin{matrix} +0.190 \\ -0.196 \end{matrix} mm/s \quad (Eq.20)$$

$$V_{3real} = 7.8 \begin{matrix} +0.124 \\ -0.073 \end{matrix} mm/s \quad (Eq.21)$$

$$V_{4real} = 3.95 \begin{matrix} +0.016 \\ -0.021 \end{matrix} mm/s \quad (Eq.22)$$

In the following, Figure 5.2 are displayed the values of the velocities found and their deviation.

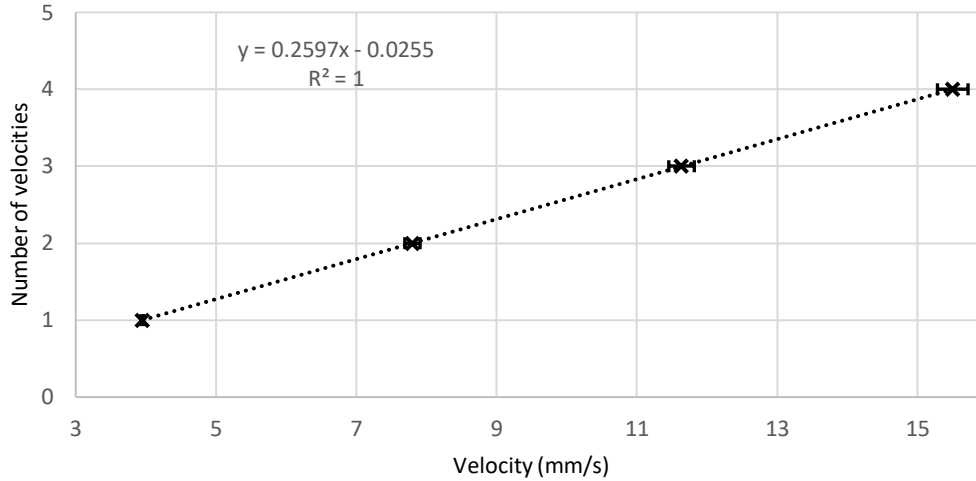


Figure 5.2 Deviation measurement for the different velocities found. [Own Source]

5.1.2. Linear Actuator feed

After estimating the 4 needle feed velocities, it was proceeded to calculate for each needle velocity configuration, the feed of the linear actuator leadscrew associated with a spindle speed of the motor. Knowing that the Nema-23 stepper motor has a step angle of 1.8° per pulse, a total of 200 pulses are required for a whole revolution. The spindle speeds programmed were converted from pulse per second to revolutions per second following (Eq.23).

$$Spindle\ speed\ \left(\frac{rev}{s}\right) = \frac{Pulse}{s} \frac{1.8^\circ}{1\ pulse} \frac{1rev}{360^\circ} \quad (Eq.23)$$

It was calculated the feed of the linear actuator by comparing each spindle speed of the motor with the needle feed velocity found, see results in Table 5.2:

$$Linear\ Actuator\ Feed\ \left(\frac{mm}{rev}\right) = \frac{Needle\ V_{real}\ \left(\frac{mm}{s}\right)}{Motor\ velocity\ \left(\frac{rev}{s}\right)} \quad (Eq.1)$$

Table 5.2 feed of the linear actuator. [Own Source]

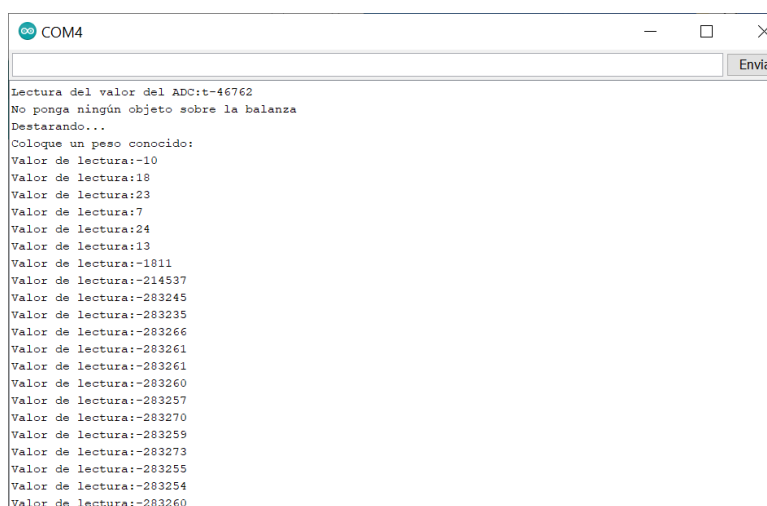
Velocities (pps)	Velocities (rev/s)	Feed (mm/rev)
200	1	3.950
400	2	3.900
600	3	3.879
800	4	3.876

The approximated feed of the linear actuator is 3.901 mm/rev, with a maximum deviation of ± 0.049 mm/rev between all feeds calculated.

5.2. Load Cell calibration

The Load Cell calibration process consisted, of finding the conversion factor between the value displayed by the load cell, and the actual weight placed on it, the Scale. This procedure needs to be done for all load cells, as every single one has its initial set scale. Without the tare, the load cell would display the deformations produced on his composing material by the weight applied to it. Different materials or geometric manufacturing conditions explain why even identical load cell models can display different deformation values with the same weight. [26]

The process started by picking a control weight, which turned out to be an iPhone 8 of 148 grams, it was proceeded to register the deformations produced by this weight with the Arduino Scale code found in Annex A4.



```

COM4
Lectura del valor del ADC:t-46762
No ponga ningún objeto sobre la balanza
Destarando...
Coloque un peso conocido:
Valor de lectura:-10
Valor de lectura:18
Valor de lectura:23
Valor de lectura:7
Valor de lectura:24
Valor de lectura:13
Valor de lectura:-1811
Valor de lectura:-214537
Valor de lectura:-283245
Valor de lectura:-283235
Valor de lectura:-283266
Valor de lectura:-283261
Valor de lectura:-283261
Valor de lectura:-283260
Valor de lectura:-283257
Valor de lectura:-283270
Valor de lectura:-283255
Valor de lectura:-283273
Valor de lectura:-283255
Valor de lectura:-283254
Valor de lectura:-283260

```

Figure 5.3 Serial Print of the scale code. [Own Source]

The average value of the control weight deformations is detailed Annex A1. The default offset for the known weight of the phone was found. Then, it was determined that the Scale with the following equation:

$$Scale = \frac{\text{Average reading value}}{\text{control weight}} = \frac{-283261.14}{180g} = -1921.12 \quad (\text{Eq.2})$$

This Scale value was included in the Force Register Code Annex A4, so that all values registered by the code displayed Mass values.

5.3. Load Cell sensitivity

5.3.1. Measurements Frequency

Because there was a delay since the load cell sends an output value until this value is displayed in the Arduino serial print. The data acquisition frequency is determined to know how many values could be recorded in one second. In case this was not fast enough, it would not be recollected enough data to make a proper analysis. After a few iterations, the Force Register Code in Annex A4 had been able to track the time the measurements were registered Annex A1.

The output results show that we can register an average of 9 measurements every second, which means that information is provided with every 0.1 s approximately. This frequency was enough, as every test was expected to last in the fastest case 1.5 s approximately. Table 5.3 shows a few time registers and their frequency, made while the load sensitivity was tested.

Table 5.3 Recording of time measurements. [Own Source]

Relative time (s)	Frequency (measurement/ second)
0.101176	-
0.202348	0.101172
0.303512	0.101164
0.404676	0.101164
0.505844	0.101168
0.60702	0.101176
0.70824	0.10122

Relative time (s)	Frequency (measurement/ second)
0.91068	0.10122
1.011936	0.101256
1.1132	0.101264
1.21446	0.10126
1.31572	0.10126
1.416984	0.101264
1.51824	0.101256
1.5	0.10126
1.72076	0.10126
1.822016	0.101256
1.923272	0.101256

5.3.2. Load sensibility

Some load sensibility tests were conducted, intending to find the minimum weight appreciable that the load cell could record. There were used different control weights of 100 g, 50 g and 5 g, made and used to calibrate digital weight scales. With the Force Register Code, Annex A4, the control weights were measured, the values recorded are found in Annex A1. Figure 5.4 shows the control loads used in the test and Figure 5.5 exhibits the weight registers are displayed in Arduino.



Figure 5.4 Control loads used in the tests. [Own Source]

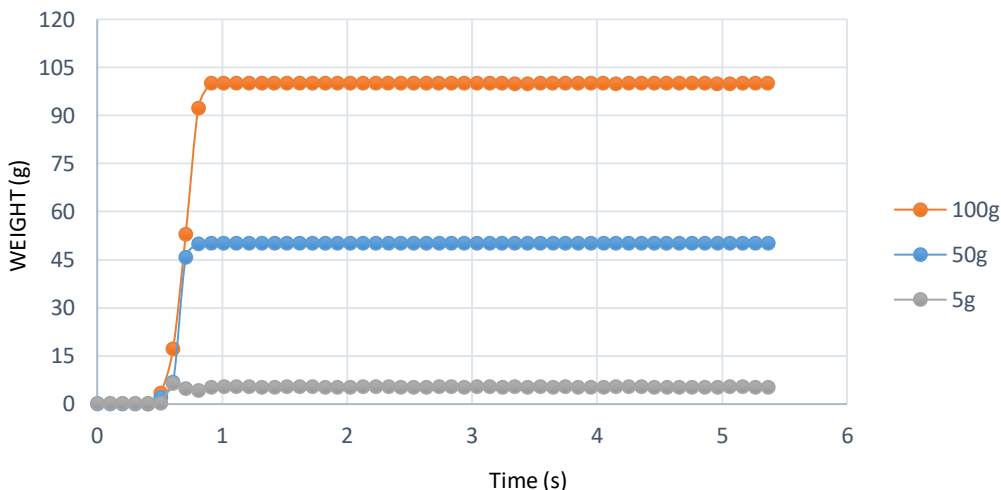


Figure 5.5 Registers of the control loads. [Own Source]

The load cell could appreciate all the control loads with no problem. The cell was observed to be sensitive to any exterior vibration produced while taking measurements. It was calculated and represented the linear error regression with the data obtained, depending on the weight. Figure 5.6 shows the error increases for smaller weights and in the smallest one 5 g. The average error was 0.37 g 0.0036 N with a deviation of ± 0.033 g. It was also found that the load cell was sensible enough, as it was not expected to register lower forces than 0.049 N

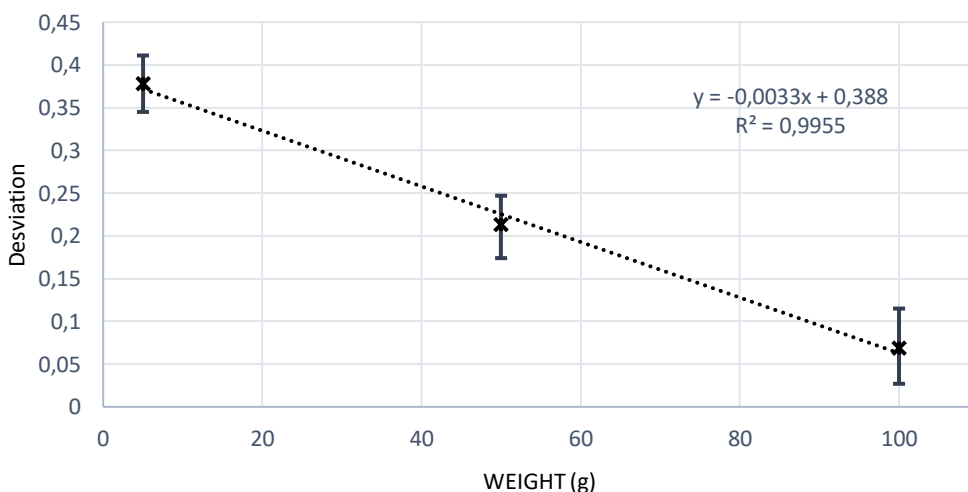


Figure 5.6 Deviation measurement for the different weight scales [Own Source]

5.4. Linear Actuator vibrations

While testing the different feed velocities, it was seen that lower velocities produced noticeable vibrations on the linear actuator. Accordingly, to check how much this behavior could affect the values registered by Arduino, it was conducted a vibration test with the app Phypox [27] and a phone attached to the linear actuator. The phone was setup to measure the x, y and z linear accelerations, excluding the gravity constant. Figure 6.7 shows the experimental setup to measure the vibration of the machine for the different feed velocities.



Figure 5.7 Setup to record vibration with the Mobil phone and the Phypox app. [Own Source]

We collected the accelerations for the fastest (15.5 mm/s) and the slowest (3.95 mm/s) feed velocity, which seemed to meet with the resonance frequency of the motor, see some of the values extracted on Annex A4. Figure 5.8 and 5.9 represent the values of the x, y and z linear accelerations 15.5 and 3.95 mm/s of feed velocities.

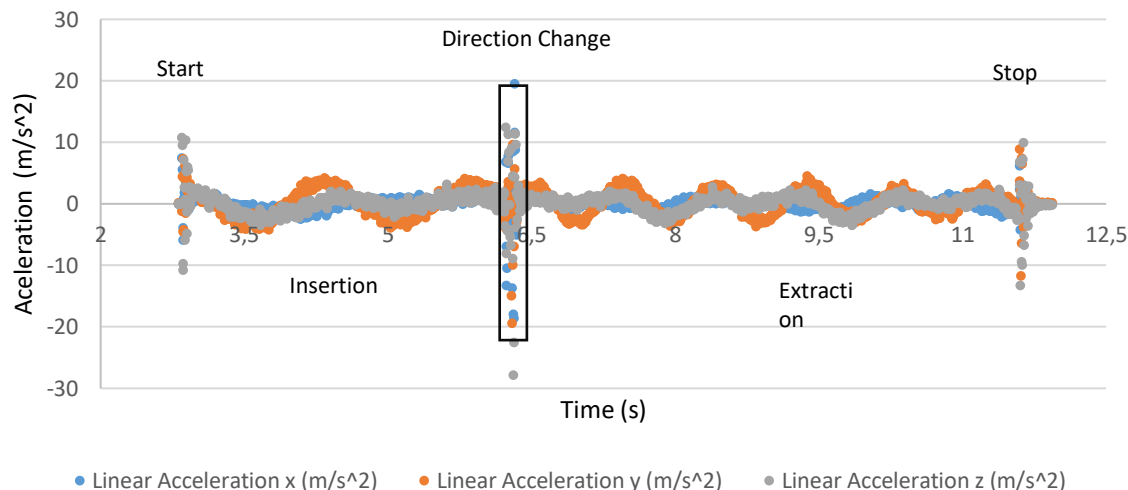


Figure 5.8 Linear accelerations when using 15.5 mm/s of feed velocity. [Own Source]

It was observed that the accelerations fluctuated along with the insertion/extraction movements of the needle. This fluctuation changed depending on the spindle speed of the motor. Also, fluctuating peaks are denoted when switching on/off the motor and when the movement direction changed.

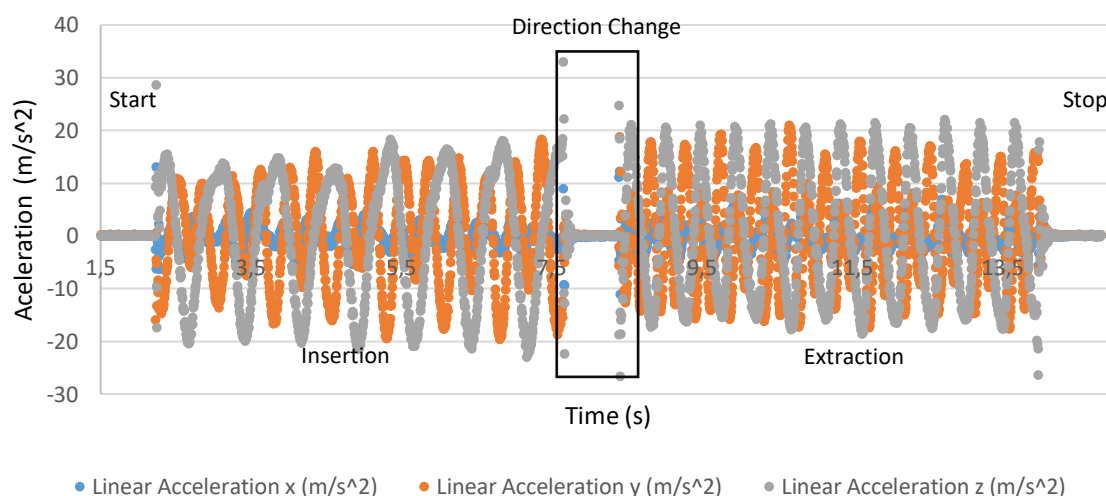


Figure 5.9 Linear accelerations when using 3.95 mm/s of feed velocity. [Own Source]

In this lower feed velocity, the vibrations achieved a larger amplitude up to 20 m/s^2 , compared with the vibrations observed when using a faster velocity. It was also found that vibrations in the Y and Z axes are much higher than in the X-axis. It was expected due to the movement contention in the YZ plane. Similar behavior was seen when switching on/off and changing the sense of the movement.

5.4.1. Vibration Analysis

The values that directly affect the registers are the linear accelerations in the Z-axis, as the load cell can only read the mass in this direction.

Table 5.4 and 5.5 show the maximum acceleration recorded during the insertion/extraction movement and the calculated incrementation of velocity that could produce per register. It was also approximated the frequency in which the maximum values of acceleration appeared, see Figure 5.10.

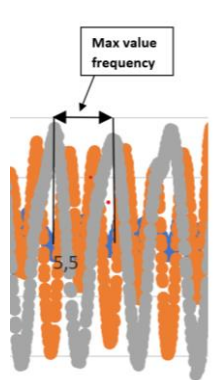


Figure 5.10 Vibration frequency when using a feed velocity of 3.95mm/s. [Own Source]

Table 5.4 Linear accelerations of the Z-axis for 15.5 mm/s of feed velocity. [Own Source]

	Linear acceleration (m/s ²)	Velocity measurement (m/s)	Max Value Frequency	Possible V. displayed (mm/s)
Max against the movement	1.6	0.0176	1.544	-2.1
Max following the movement	2.11	0.02321	1.4	38.71

Table 5.5 Linear accelerations of the Z-axis for 3.95 mm/s of feed velocity. [Own Source]

	Linear acceleration (m/s ²)	Velocity measurement (mm/s)	Max Value Frequency	Possible V. displayed (mm/s)
Max against the movement	17.57	0.19327	0.7441	-189.32
Max following the movement	23.08	0.25388	0.7542	257.83

Quantifying the maximum amount of velocity that could increase and decrease during the experiments, let the understanding that for a feed velocity of 3.95 mm/s (producing larger vibrations), some recorded values would not behave as expected vibration could modify the desired feed velocity. Assuming the worst-case scenario, the error could affect 2 values out of 9 per second.

On the contrary, for the highest feed velocity (15.5 mm/s), the maximum and minimum influence on velocity due to vibration was not as high, and the frequency in which these occurred was much slower. Because of its slow frequency, we could predict that a maximum of 2 values out of 14 registers could be appreciated out of the tendency.

Several peaks of the linear accelerations were observed when switching on/off and changing the movement direction. However, these peaks produced will not be considered in the insertion/extraction analysis because we aim to study the needle's interaction and its movement when penetrating a specific tissue.

5.4.2. Testing results

Figure 5.11 represents non-processed values, extracted from a 27G needle test at 3.95mm/s feed velocity on a Biological tissue. As can be seen in the graph, there are minimum picks of force during the insertion. As described before, those are attributed to the vibrations produced by the lowest velocity.

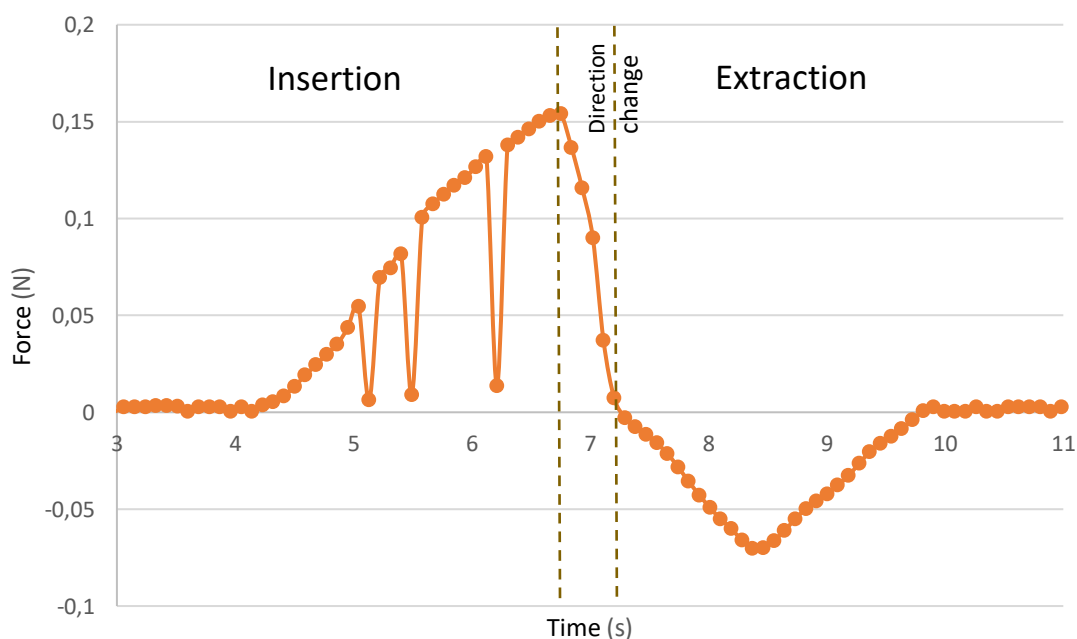


Figure 5.11 Non-processed force values during the needle insertion and extraction cycle when using a 27G needle and a feed velocity of 3.95 mm/s. [Own Source]

This phenomenon repeated along the tests carried out with 3.95mm/s feed velocity. The errored values, caused by the spindle rotation of the motor, display only as minimum peaks of force in the insertion process. It is expected when considering that the effects of maximum accelerations against the movement, can be smoothed by the inertia of the moving needle supports of the linear actuator, which includes its weight and the weight of a motor and the needle holder.

5.5. Needle Angle determinations

The hypodermic needle fabricant did not provide any specifications about the needle bevel type and angles, as this is an influential parameter on the forces produced in the insertion process, it was characterized the bevel type by taking pictures of each needle tip, with an electronic microscope and a scale, and measuring the bevel length and angle with a windows application called Gimp2 [28]. This app lets us define the relative angles and pixel measurements from the photos displayed in Annex A1. Figure 5.12 shows a ruler scale used to find the conversion between mm and pixels.

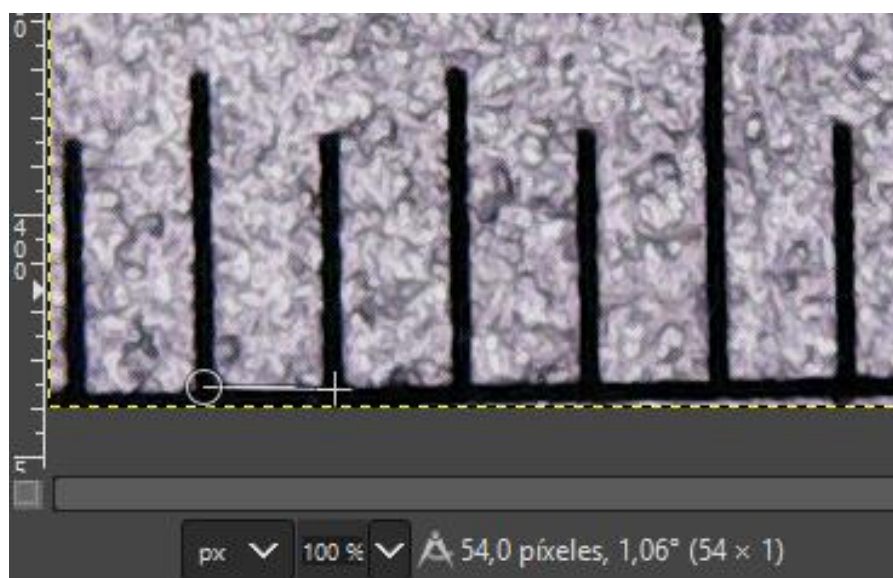


Figure 5.12 Gimp2 capture displaying the conversion between pixels to mm. [Own Source]

Figure 5.13 exhibits how it was taken the needle's inclination angle before taking the bevel angle measurements. All needles had a small inclination angle from the X-axis that had to be considered to estimate the bevel angles. While, Figure 5.14 shows the needle's tip measurements in different positions to measure the bevel length and angles.

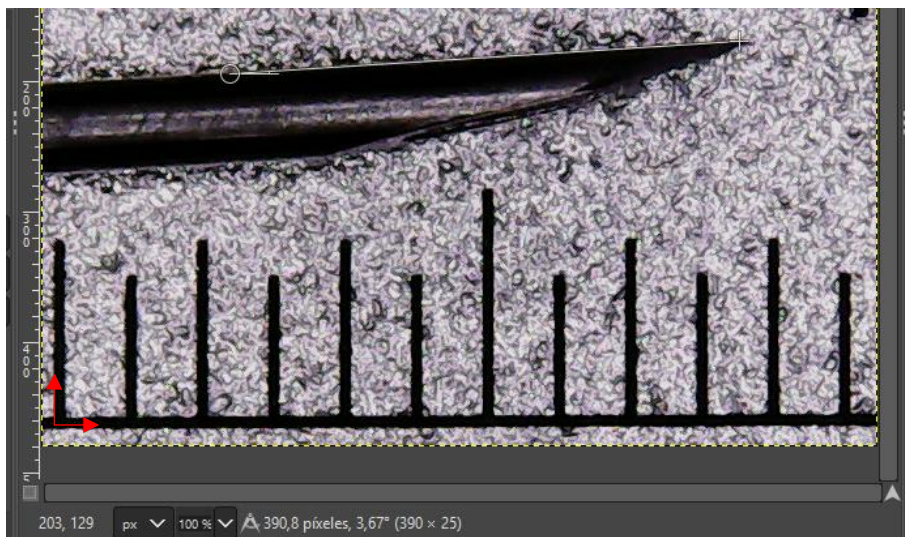


Figure 5.13 Gimp2 capture with the inclination angle of the ruler. [Own Source]

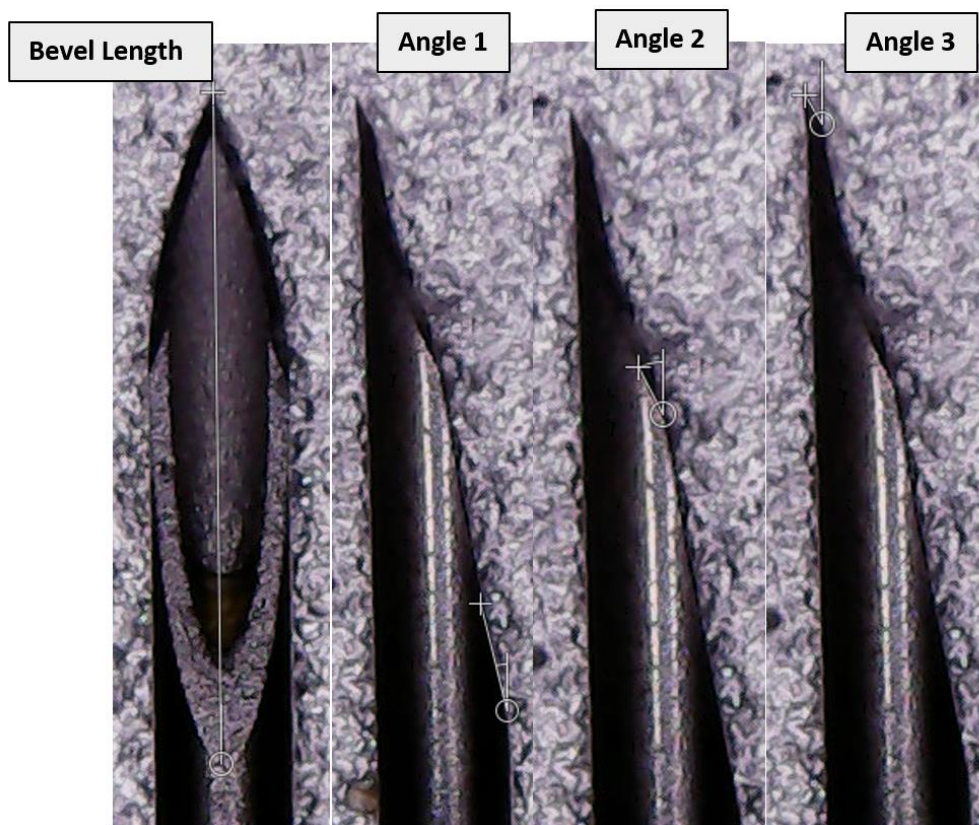


Figure 5.14 Gimp2 capture that shows the bevel length and bevel angles. [Own Source]

It was denoted that all needles had the same bevel type, composed of the 3 bevel angles. Table 5.6 gathers all lengths and bevel angles measured for each needle tested. The needle angles present similar values between the different needle ranges, although some differences are found. These

differences could be due to human errors while measuring the angles and the manufacturer's fabrication tolerances.

Table 5.6 Bevel length and angle measurements. [Own Source]

Needle Type	Length	Angle1	Angle2	Angle3
18g	8.03	12.21	19	24
20g	7.5	12.8	17	23.6
21g	7.5	13	20	24.44
22g	6.18	12.31	18	24.7
23g	6.2	12	17	23
25g	4.6	12.95	16.24	26
27g	3.5	12.8	15.6	25
30g	2.5	13	16.3	23
Average value ± Standard deviation		12.63 ±0.4	17.39 ±1,55	24.21 ±0.98

6. Methodology

This methodology aims to guide the usage of the experimental bench and state the bases for future experimental procedures.

6.1. Control Variables

Between all different factors that influence the insertion forces, the tests done in this paper are designed to describe the influence of:

- Different needle diameters
- Bevel angles of the needle tips
- Feed velocity of penetration

The control parameters for these factors are the following ones:

Diameter analysis

- Same needle type with different diameters.
- Same velocity of penetration.

Tip type analysis

- Same diameter needle with a different tip regarding the bevel angles
- Same velocity of penetration.

Velocity analysis

- Same needle for all cases
- different feed velocities.

During the experiments, other parameters needed to be considered. Firstly, it had to be ensured that all biological samples presented a certain homogeneity and they had been kept on the same refrigeration conditions for every set of experiments. Also, it was recorded the relative time associated with every force register made. This time enabled the taking of the needle's position in every register.

6.2. Materials

6.2.1. Hypodermic needles

All the needles used were hypodermic needles from *BC Mricolance*. The different gauges were provided: 18G, 20G, 21G, 22G, 23G, 25G, 27G, 30G. Table 6.1 lists the diameter and dimensions of the different needles used in this project. See the different colors assigned for each type and specifications of the package, see Figure 6.1.



Figure 6.1 Type of needles used in its package. [Own Source]

Table 6.1 Needle package geometrics specifications. [Own Source]

NEEDLE TYPE	DIAMETER (mm)	NEEDLE LENGTH (mm)
18G 1/2"	1.2	40
20G 1"	0.9	25
21G 1"	0.8	25
22G 1 1/4"	0.7	30
23G x1"	0.6	25
25G x 5/8"	0.5	16
27G 1/2"	0.4	13
30G 1/2"	0.3	13

The bevel type for this needle is called back needle, they are commonly used in hypodermic needles. Figure 6.2 shows how the needle tip looks like and its different parts.

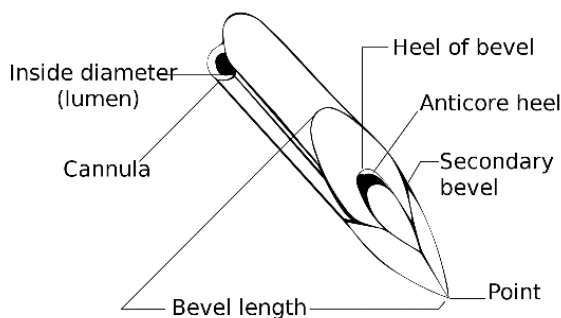


Figure 6.2 Needle bevel features. [29]

An optical microscope was used to determine the main bevel features of the needles. This type was composed of three bevel angles, see Figure 6.3. In Table 6.2, there is the resume of the three bevel angles and the bevel's length.

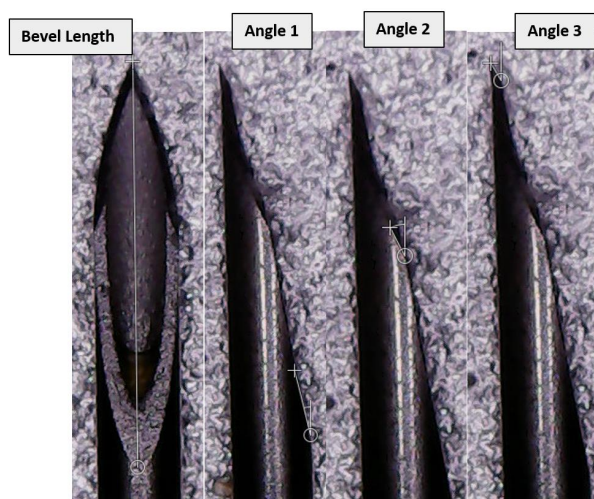


Figure 6.3 Grimp2 capture that shows the bevel length and bevel angles. [Own Source]

Table 6.2 Needle bevel angles. [Own Source]

Needle type	Bevel length (mm)	Angle1	Angle2	Angle3
18G 1/2"	8.03	12.21	19	24
20G 1"	7.5	12.8	17	23.6
21G 1"	7.5	13	20	24.44
22G 1 1/4"	6.18	12.31	18	24.7
23G x1"	6.2	12	17	23
25G x 5/8"	4.6	12.95	16.24	26
27G 1/2"	3.5	12.8	15.6	25
30G 1/2"	2.5	13	16.3	23

The needle angles present similar values between all needles, although some differences were found. These differences can be attributed to human errors while measuring the angles or to the manufacturer's fabrication tolerances.

6.2.2. Biological tissue

The biological tissue used for the first experiments were some chicken breasts, bought fresh from a supermarket the same day that the tests were carried out, and conserved on a fridge at a temperature of 8°C.

6.2.3. Sample recipient

For this experiment set, the recipient used to retain the samples where a one-use flat plastic glass. It was selected this type, because its flat base and straight walls, would not interfere with the tissue, compressing it and modifying its viscoelastic properties.

6.3. Experimental procedure

6.3.1. Machine setup and sensors calibration

- It must be ensured that the load cell is centered on the axis of the needle adapter. See Figure 6.4.

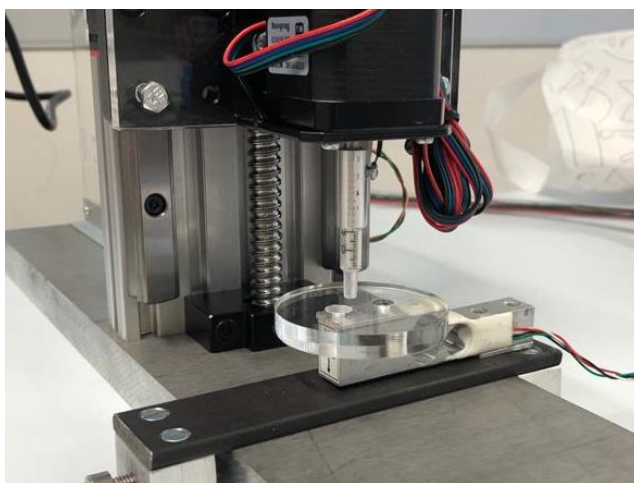


Figure 6.4 Pick of the centered load cell with the needle. [Own Source]

- The limit switches sensors must be strategically sated up for the experiment. The length of the needle tested must be taken into consideration when placing the sensors. This step must be repeated every time the length of the needle changes substantially.

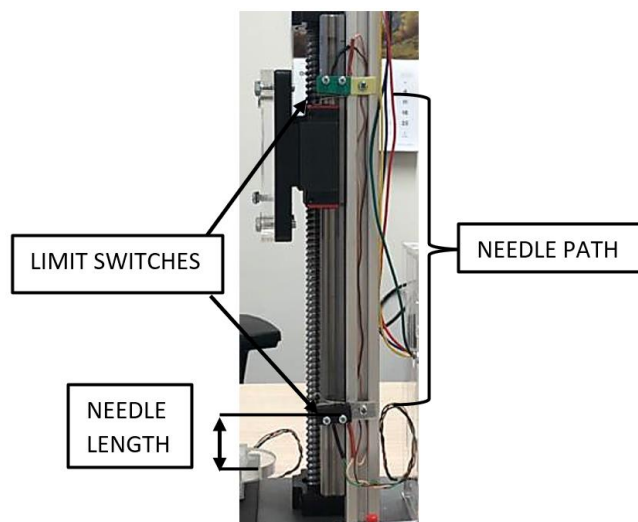


Figure 6.5 Limit switches placed on the linear actuator. [Own Source]

- The limit switches are placed and the movement of the motors must be tested for each velocity, see Figure 6.6. All for velocities must be selected following the binary matrix, shown below:

$$\begin{pmatrix} 00 & 01 \\ 01 & 11 \end{pmatrix} = \begin{pmatrix} V_1 & V_2 \\ V_3 & V_4 \end{pmatrix} = \begin{pmatrix} 15.5_{mm/s} & 11.6_{mm/s} \\ 7.8_{mm/s} & 3.95_{mm/s} \end{pmatrix} \quad (Eq.3)$$

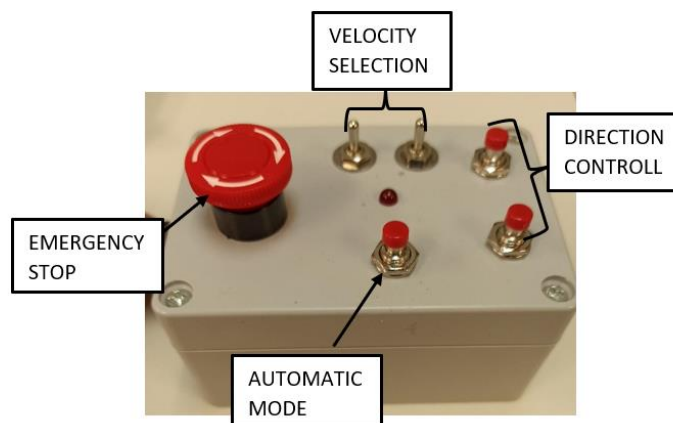


Figure 6.6 Button box controller. [Own Source]

6.3.2. Tissue sample preparation

- The tissue samples must be cut to a size that fits into the plastic glass, they must be placed flat in the recipient. See Figure 6.7.



Figure 6.7 Prepared chicken breast sample. [Own Source]

- The load cell Arduino nano must be plugged into a Laptop and checked out that these two communicate properly, running the force measuring code found on Annex A4. See the procedure in Figure 6.8 and 6.9.

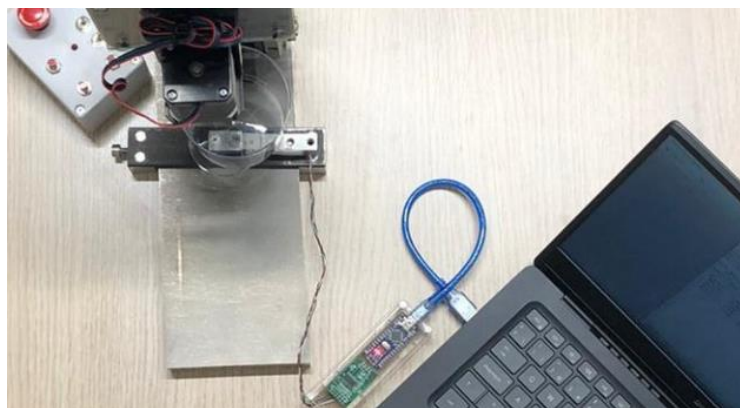


Figure 6.8 Connected load cell to a pc. [Own Source]

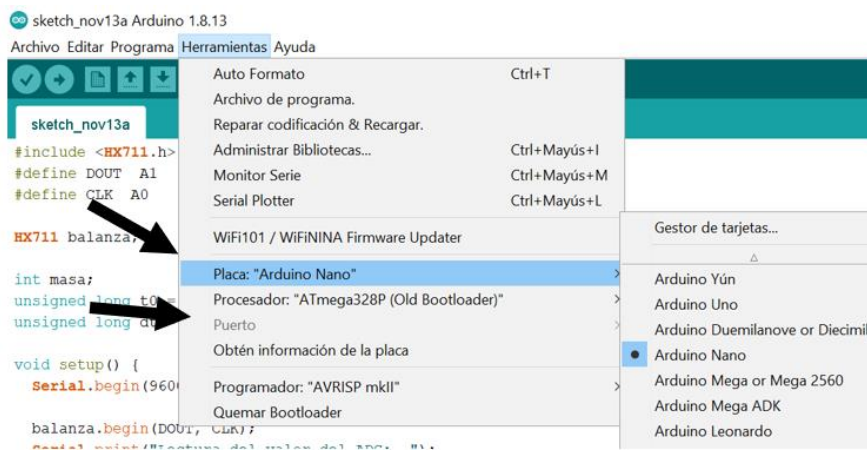


Figure 6.9 Arduino settings for troubles with USB port. [Own Source]

- The next step is to take the tissue sample's weight with Arduino. Once the Arduino COM is displaying values, the tissue sample must be placed on the load cell. Two columns of numbers will appear on the COM: the time (μs) and weight value (centigrams), see Figure 6.10.

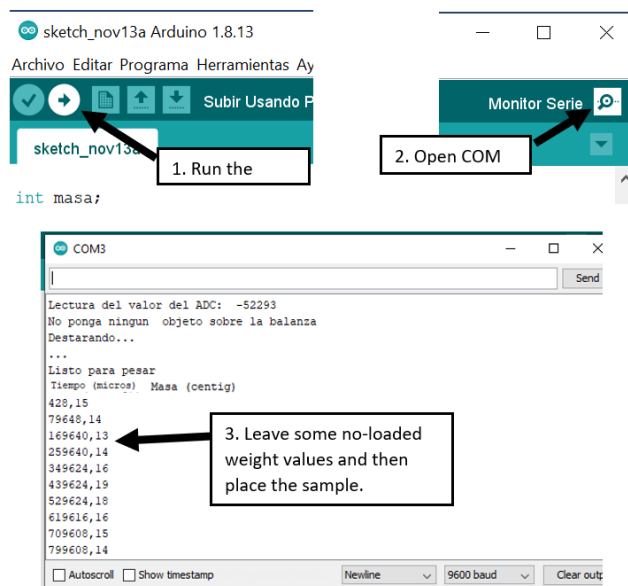


Figure 6.10 Arduino steps to start taking measurements. [Own Source]

6.3.3. Needle placing

- The plastic glass with the prepared tissue sample must be centered in the methacrylate plate of the load cell.
- It must be ensured that the needle is placed parallel to the linear actuator, there must be some space between the needle tip and the sample tissue, so for every test, it can be registered some data with no load in it, see Figure 6.11.

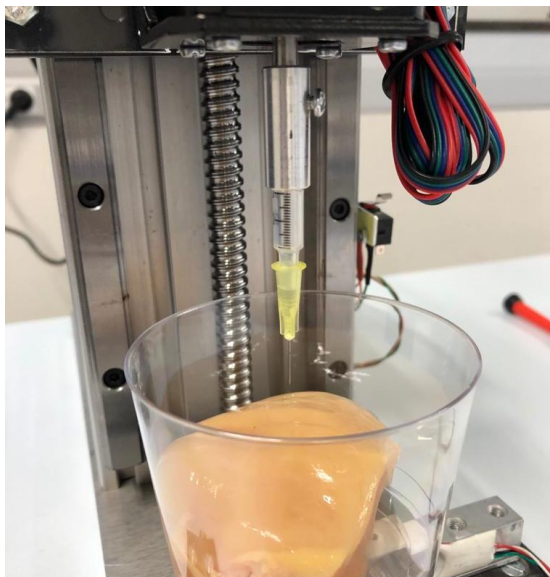


Figure 6.11 30G needle set up, ready to take measurements. [Own Source]

6.3.4. Test procedure

- Select the desired velocity on the control box, see Figure 6.6.
- Run the code force registering code, and open the COM, once this starts displaying measurements, press the down button on the control box to initialize the movement of the needle.
- Once you see that the needle is halfway down into the sample, press the up button to change the movement to register the friction forces produced.
- When the needle tip gets out of the tissue, wait for a few seconds, and press the emergency stop button.
- Copy the data from the Arduino COM to an excel sheet for postprocessing of the values.
- Move the sample glass slightly to one side, so the next penetration is not made on the same spot.
- Unplug the emergency button, and repeat the same procedure done.

The sample needs to be changed every few insertions to avoid making two insertions in the same spot. Figure 6.12 shows the tissue's behavior during the experiment, where the deformations of the tissue are denoted during the insertion or retraction.

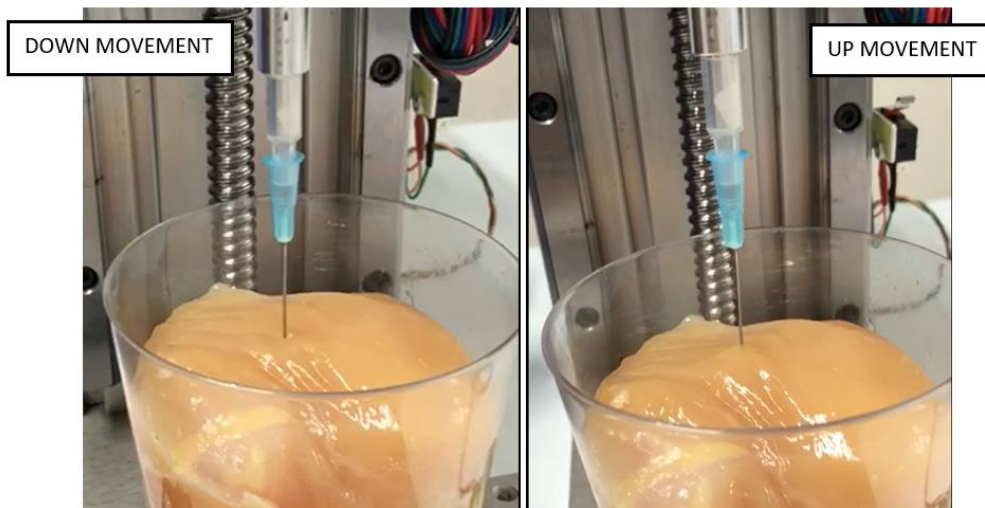


Figure 6.12 25G needle insertion and extraction. [Own Source]

6.3.5. Experiment wrapping procedure

- The machine must shut down and unplugged.
- The load cell must be carefully unplugged from the laptop.
- Any possible dust coming from the biological tissue must be cleaned with some alcohol-based cleaner.

7. Data analysis and preliminary results

7.1. Data acquisition and calculations

The values provided from Arduino were gathered in an excel sheet to start with the calculation. In Annex A2, are displayed the tables and figures of each register made for the 32 tests. Two column arrays were recorded during the experiments, the Mass (cg) registered by the load cell and the time (μ s) by the Arduino code. Both values were synchronized since code started displaying values in its port. After collecting the data, it was necessary to postprocess and remove non-essential values, such as initial unloaded values, only to analyze the insertion and extraction cycle. We also removed the errored values produced by the vibrations in some velocities. Table 7.1 shows the load and time values recorded from the Arduino copied to excel during the initial part of an insertion cycle.

Table 7.1 Time and force values during an insertion process with 30G needle and a feed velocity of 15,5 mm/s [Own Source]

Velocity (mm/s)	15,5
Time (μ s)	Mass (cg)
4221980	21
4312036	49
4402076	241
4492120	488
4582164	590
4672208	672
4762248	811
4852284	918
4942320	853
5032360	173
5122404	-305
5212440	-493
5302484	-446
5392520	-353
5482556	-281
5572604	-173
5662648	-38
5752688	17

From these time and mass values, it was calculated a column with the relative time of the insertion-extraction cycle, and the with needle's feed velocity, it was also estimated the relative position of the needle.

$$Time_{rel(i)} = t_i - t_0 \quad i = 1,2,3,4.. \quad (Eq.4)$$

$$Pos_{rel(i)} = T_{rel(i)} V_{needle(n)} \quad i = 1,2,3,4.. \quad (Eq.5)$$

$$n = 3.95, 7.8, 11.6, 15.5$$

The axial movement of the needle matched with the gravity direction, due to the 90° insertion angle. That is why the axial force was calculated by multiplying the recorded Mass by the gravity constant.

$$F_{axial(i)} = Mass_{(i)} g \quad i = 1,2,3,4.. \quad (Eq.6)$$

After postprocessing, Table 7.2 exhibits the relative time, position and force when using a 30G needle and a 15.5 mm/s feed velocity. The green cells mark the unloaded values left at the beginning and end of the tests.

Table 7.2 Postprocessed values of time, position and force when using 30G needle and a feed velocity of 15.5 mm/s. [Own source]

Time (μs)	Mass (cg)	Time rel. (s)	Pos rel. (mm)	Force(N)
4221980	21	0	0	0.0020601
4312036	49	0.090056	1.395868	0.0048069
4402076	241	0.180096	2.791488	0.0236421
4492120	488	0.27014	4.18717	0.0478728
4582164	590	0.360184	5.582852	0.057879
4672208	672	0.450228	6.978534	0.0659232
4762248	811	0.540268	8.374154	0.0795591
4852284	918	0.630304	9.769712	0.0900558
4942320	853	0.72034	11.16527	0.0836793
5032360	173	0.81038	12.56089	0.0169713
5122404	-305	0.900424	13.956572	-0.0299205
5212440	-493	0.99046	15.35213	-0.0483633
5302484	-446	1.080504	16.747812	-0.0437526
5392520	-353	1.17054	18.14337	-0.0346293
5482556	-281	1.260576	19.538928	-0.0275661
5572604	-173	1.350624	20.934672	-0.0169713
5662648	-38	1.440668	22.330354	-0.0037278
5752688	17	1.530708	23.725974	0.0016677

The insertion force and the relative time calculated were visualized, to determine the different parts of the interaction between the needle and the soft tissue. Figure 7.1 shows all the phases of needle insertion and extraction. The force values during the extraction are negative because the movement of the needle was against the direction of gravity.

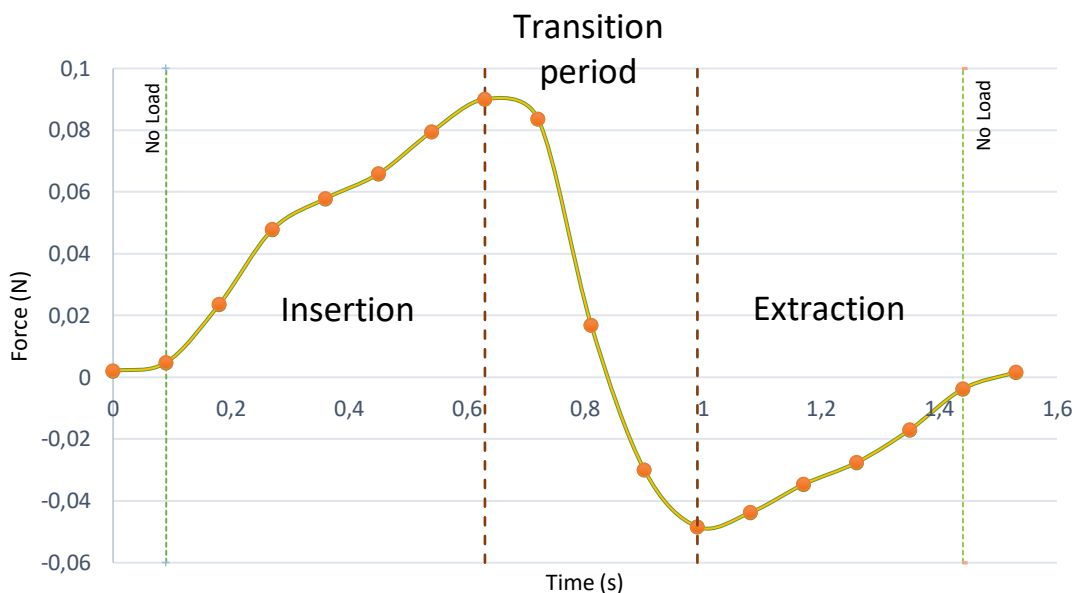


Figure 7.1 Table 1: Force behavior during the needle insertion and extraction cycle when using a 30G needle and a feed velocity of 15.5 mm/s. [Own Source]

Between the insertion and the extraction, it has been distinguished a transition period related to the direction change of the needle. The force values were expected to drop as the movement direction changed, but a transition slope was observed, attributed to the tissue relaxation produced on soft-tissues because of its viscoelastic properties. When the needle changes the movement direction, the compression applied to the tissue disappears, and the layers relax and accommodate along the superficial area of the inserted needle. This accommodation phenomenon of the layers, produces an opposing force to the needle, making the values of the force drop down slowly.

7.2. Cutting and Friction forces

Thanks to the previous figure, we were able to find the maximum cutting force ($F_{cutmax} + F_{fricc max}$), corresponding to the maximum value on the insertion period. During the insertion phase, the penetration and friction forces were registered together, because while the needle tip is cutting layers of tissue, the surface area of the needle inserted is submitted to some friction from the tissue already cut. We also obtained the maximum friction force ($F_{fric max}$) with the maximum value on the needle extraction period. Figure 7.2 shows the insertion and extraction values to compare the force values of the cutting and friction forces during the experiment.

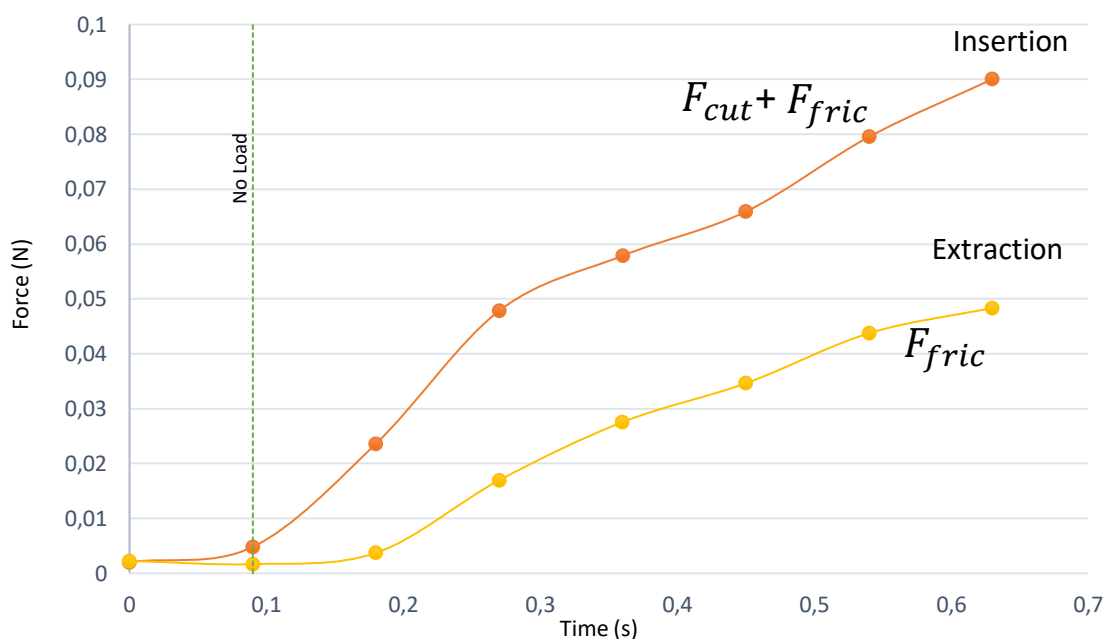


Figure 7.2 Cutting and friction forces when using a 30G needle and a feed velocity of 15,5 mm/s. [Own Source]

Table 7.3, lists the insertion and extraction force values related to the same sequence of time used to represent Figure 7.2. Also, Table 7.4 displays the maximum values of F_{cutmax} , $F_{fricc max}$ when using a 30G needle and a feed velocity of 15.5 mm/s.

Table 7.3 insertion and extraction force values listed values when using a 30G needle and a feed velocity of 15.5 mm/s. [Own Source]

Rel. Time (s)	Insertion Force (N)	Extraction Force (N)
0	0.0020601	0.0022563
0.090056	0.0048069	0.0016677
0.180096	0.0236421	0.0037278
0.27014	0.0478728	0.0169713
0.360184	0.0578790	0.0275661
0.450228	0.0659232	0.0346293
0.540268	0.0795591	0.0437526
0.630304	0.0900558	0.0483633

Table 7.4 F. Cutting max, F. friction max when using a 30G needle and a feed velocity of 15.5 mm/s. [Own Source]

F. Cutting max (N)	0.0416925
F. Friction max (N)	0.0504234

7.3. Stiffness force

The stiffness force accounts for the force to overcome the tissue's superficial tension, and the start of the interaction between the needle and the inner tissue layers produces a different pendent of the insertion force. Theoretically, it should be a peak of force, as seen before with the maximum cutting force, but in the experiment, all we found was a change of tendency in the force curve. In Figure 7.3, the change of tendency is denoted at the beginning of the insertion, due to the superficial stiffness.

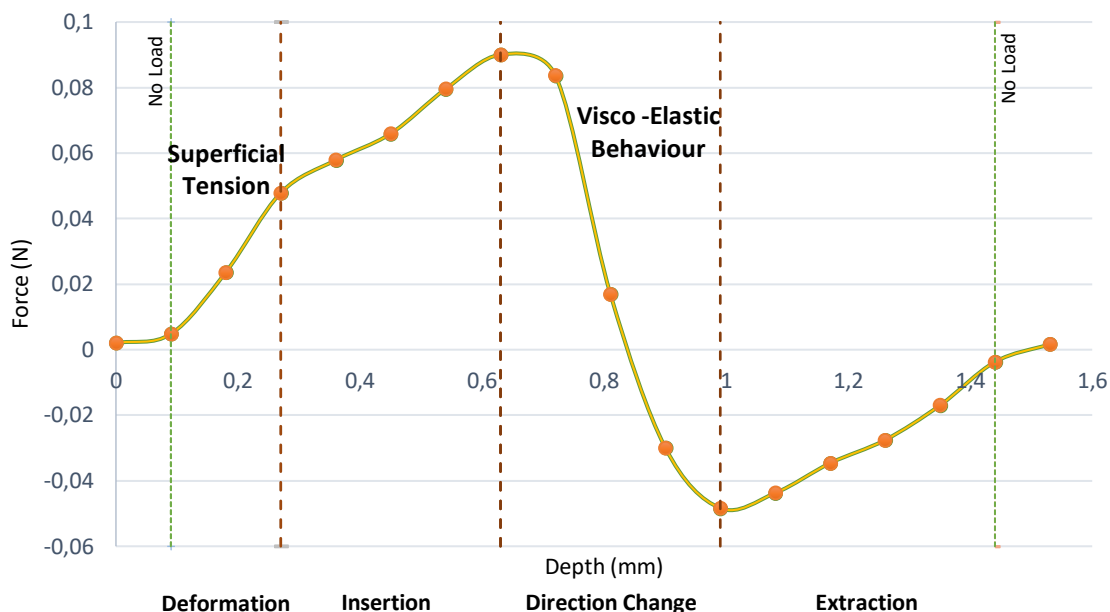


Figure 7.3 Force behavior during the needle insertion and extraction cycle when using a 30G needle and a feed velocity of 15.5 mm/s. [Own Source]

In this case, the change of tendency was evident, and it was determined a $F_{stiffnes} = 0.04581 N$. But the change of tendency turned less clear for higher velocities, as we were able to register more values and the changes were not as drastic. Figure 7.4 denotes a not evident change of the insertion force tendency due to using a feed velocity of 3.95 mm/s.

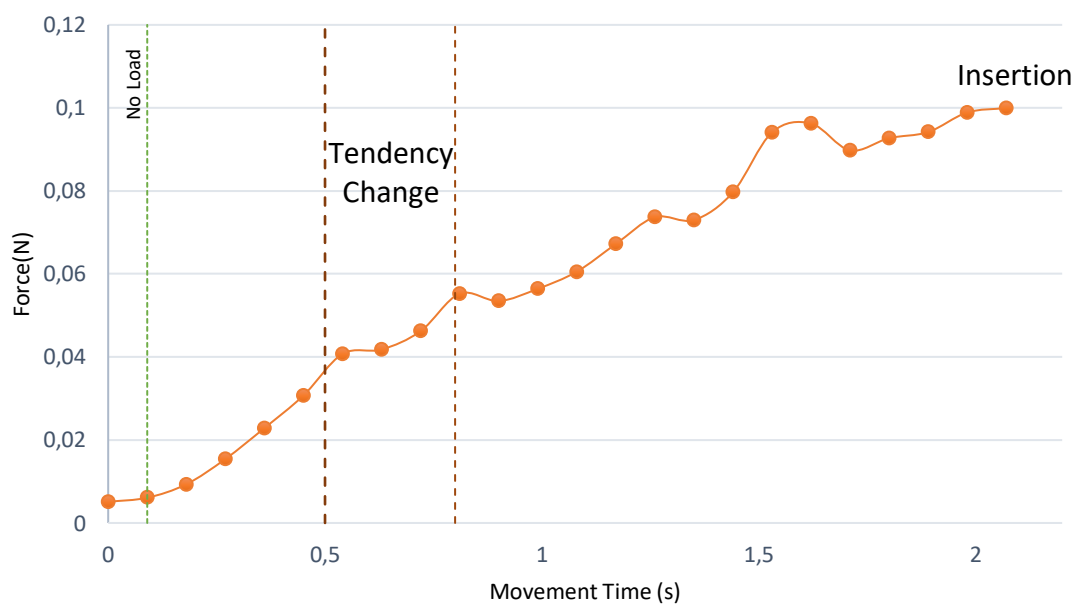


Figure 7.4 Insertion forces when using a 30G needle and a feed velocity of 3.95 mm/s. [Own Source]

7.4. Superficial Deformation

Having already extracted the $F_{stiffness\ max}$, it was calculated the approximated axial deformation of the tissue while there was no penetration. This was done by calculating the needle tip position for the value of the Superficial Deformation

$$Superficial\ Deformation_{(n)} = Time_{(F_{stiffness\ max}(n))} V_{needle(n)} \quad (Eq.7)$$

$$n = 3.95, 7.8, 11.6, 15.5$$

For the case of a 30G needle at 15.5mm/s, $Deformation = 2.791\ mm$. This value is approximated, as it is assumed that the insertion of the needle is constant during the time, and it may not be the exact cause. For future experiments, the extraction of the deformation and the movement should be tracked by a camera.

7.5. Cutting force per Depth

As the length of each needle changed, we could not ensure that the maximum value of friction and the cutting forces, corresponded to the same depth for each needle tested, adding that the insertion values recorded included the deformation of the tissue. That is why to analyze the cutting forces its values were compared to the depth perforated for each.

The actual depth penetration was found from the needle extraction values. As to the insertion, the time recorded not only refers to the penetration, but also the tissue deformation. In the extraction, values only correlate with the depth perforated. Following the next equation, the cutting force per depth was found:

$$Cutting\ Force\ per\ Depth_{(i)} = \frac{F_{cutting\ max(i)}}{\left(Time_{(F_{friction(i)})} V_{needle(n)} \right)} \quad i = 1,2,3,4.. \quad (Eq.8)$$

$$n = 3.95, 7.8, 11.6, 15.5$$

For its proper calculation, it must be taken into consideration the stiffness force and the position where the penetration started. Table 7.5 displays the calculations made for a 30G needle and a feed velocity of 15.5mm/s.

Table 7.5 Cutting Force per Depth listed calculation when using a 30G needle and a feed velocity of 15.5 mm/s [Own Source]

Depth (mm)	F. cutting/depth (N/mm)
9.769	0.004
8.374	0.004
6.978	0.004
5.583	0.005
4.187	0.007

7.6. Friction per Unit of Contact Area

For the same reason of calculating the cutting force per unit length, it was needed a parameter that displayed the friction values per unit of contact area, between the needle and the tissue. Consequently, for each friction parameter, we calculated an approximate area of contact for each needle type and velocity with the following formula:

$$\text{Friction per Contact Area}_{(i)} = \frac{F_{fricc(i)}}{(2\pi r L_{(i)})} \quad i = 1,2,3,4.. \quad (\text{Eq.9})$$

Being r the external radius of each needle and L the depth perforated. As expected, this value remained constant along with the extraction, for each needle type and feed velocity.

shows the friction per contact area values when using a 30G needle and a feed velocity of 15.5 mm/s.

Table 7.6 Friction per Contact Area listed calculation when using a 30G needle and a feed velocity of 15.5 mm/s [Own Source]

Depth perforated (mm)	Friction Force (N)	Contact Area (mm ²)	Friction per Contact Area (N/mm ²)
0	0.0022563	-	-
1.395868	0.0016677	-	-
2.791488	0.0037278	2.630681724	0.000633942
4.187170	0.0169713	5.261480314	0.002834031
5.582852	0.0275661	7.892395772	0.003231718
6.978534	0.0346293	10.52296063	0.003095061
8.374154	0.0437526	13.15352548	0.003169683
9.769712	0.0483633	15.78432408	0.002933493

7.7. Results

For all the 32 tests that have been calculated the values of stiffness force, deformation, maximum cutting and friction force, the cutting force per depth and the friction per contact area. All of them were gathered in Table 7.7 for a proper analysis between the parameters that affect this value. See all the values extracted on the experimental procedures on Annex A2.

Table 7.7 F.stiffnes, Deformation, F. cuttin max, F.friction max and friction per contact unit, for all tests.

[OwnSource]

Diameter (mm)	Feed Velocity (mm/s)	F. Stiffness (N)	Superficial Deformation (mm)	F. Cutting max (N)	Max F. Cutting per depth (N/mm)	F. Friction max (N)	Friction per Contact Area (N/mm ²)
0.3	15.50	0.04581	2.79130	0.04169	0.004268	0.05042	0.00293
	11.60	0.04473	2.08856	0.06239	0.009958	0.04091	0.00295
	7.80	0.03904	1.40459	0.05140	0.008133	0.06023	0.00404
	3.95	0.03561	1.77837	0.05160	0.010363	0.05346	0.00496
0.4	15.50	0.06622	2.79105	0.05199	0.006209	0.06995	0.00336
	11.60	0.06975	3.13353	0.06749	0.00718	0.09722	0.00388
	7.80	0.07004	4.21412	0.06553	0.007775	0.08721	0.00407
	3.95	0.06592	3.55647	0.08358	0.014688	0.07397	0.00498
0.5	15.50	0.07387	4.18686	0.05405	0.004841	0.14695	0.00407
	11.60	0.05837	3.13372	0.05778	0.005532	0.11674	0.00357
	7.80	0.07044	4.21409	0.04827	0.005286	0.12017	0.00411
	3.95	0.04415	3.20108	0.07828	0.00957	0.10075	0.01702
0.6	15.50	0.13037	5.58248	0.06524	0.003595	0.17295	0.00269
	11.60	0.08741	4.17772	0.06023	0.003845	0.18502	0.00317
	7.80	0.12272	6.32084	0.08996	0.008005	0.15519	0.00349
	3.95	0.11154	6.75813	0.10045	0.008558	0.19463	0.00451

Diameter (mm)	Feed Velocity (mm/s)	F. Stiffness (N)	Superficial Deformation (mm)	F. Cutting max (N)	Max F. Cutting per depth (N/mm)	F. Friction max (N)	Friction per Contact Area (N/mm ²)
0.7	15.50	0.17177	11.16564	0.14087	0.00721	0.28675	0.00361
	11.60	0.15716	8.35557	0.11517	0.006892	0.21955	0.00293
	7.80	0.13597	7.02362	0.11232	0.007997	0.17766	0.00275
	3.95	0.06926	4.62368	0.10428	0.012748	0.13116	0.00340
0.8	15.50	0.16491	9.76922	0.12900	0.007702	0.19718	0.00344
	11.60	0.16393	8.35562	0.11644	0.006558	0.21808	0.00244
	7.80	0.21386	9.83206	0.14843	0.009188	0.23377	0.00281
	3.95	0.11085	7.11333	0.10320	0.008534	0.19846	0.00311
0.9	15.50	0.24937	9.76891	0.08397	0.005015	0.24859	0.00250
	11.60	0.16736	6.26725	0.10673	0.007299	0.21906	0.00256
	7.80	0.16481	7.02356	0.11056	0.008284	0.24319	0.00312
	3.95	0.06710	10.66995	0.16883	0.017581	0.17835	0.00340
1.2	15.50	0.29146	9.76940	0.18757	0.010338	0.27193	0.00207
	11.60	0.14823	4.17795	0.25604	0.018857	0.25869	0.00239
	7.80	0.13656	4.91625	0.19149	0.017041	0.29528	0.00350
	3.95	0.09398	3.55644	0.25329	0.030966	0.21533	0.00363

For all Data recollected in the previous Table 7.7, in the following part of the chapter, these values will be represented in different graphs. Divided by the parameters calculated, these are represented regarding the diameter of the needle, and the different velocities tested. In this way, it is intended to find some relation between these parameters in a needle's insertion cycle and the tests'- controlled parameters.

We are talking about really small amounts of force (a maximum of 0.3N), which in some cases could be interpreted as constant along with the different tests. The linear regressions for 3.99mm/s and 15.5 mm/s velocities in the graphs, intend to be a tool to help analyze the velocities impact,

although its behavior may not be linear. The intermediate feed velocities linear regression had not been displayed because of the proximity of the results obtained for these two.

7.7.1. Superficial Deformation

Figure 7.5 displays the superficial deformations of the tissues while being tested. It can be seen an increasing tendency of the needle diameters' deformations, attributed to the contact area of the needle tip, as it increases for higher diameters. Although it looks like from the 0.7 mm to 1.2 mm diameter, the incrementations of the deformation values hold back and remain approximately the same for the rest of the diameters.

With the help of linear regression, it has been distinguished, a not so clear incrementation of the deformations from the lowest to highest feed velocities. It is seen how on lower needle diameters (0.3 mm, 0.4 mm), the influence of velocities in the deformations is not as evident as for higher diameters (0.7 mm, 0.9 mm). The variance of deformation values from 0.7 to 1.2 mm diameters is higher. This incrementation of velocity influence could be attributed to the deviation. The values obtained for the 1.2 mm diameter needle for the 11.6, 7.8, 3.95 mm/s velocities suddenly drop out of the tendencies expected.

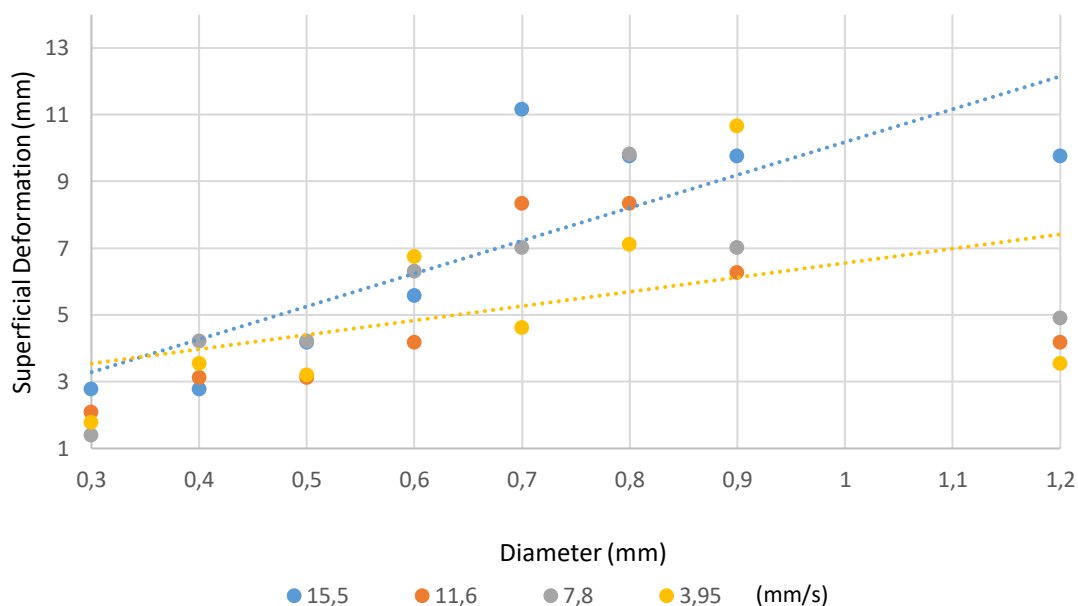


Figure 7.5 Superficial Deformations produced for each needle and feed velocity. [Own Source]

7.7.2. Stiffness force

The stiffness force represented in Figure 7.6 presents a clear incrementation on the stiffness force with the incrementation of the insertion velocities. The tissue's viscoelastic properties explain this and its increment of resistance by the incrementation of acceleration applied.

Regarding the diameter, we have seen that this parameter has a clear influence in the highest velocity, 15.5 mm/s, with a difference of 0.25 N between the 0.3 mm diameter and 1.2 mm. But in the lowest one, 3.95 mm/s, the difference between the biggest and the smallest diameter is about 0.05N. This insignificant incrementation of force exhibits that the velocity is slow enough to make the tissue stiffness force behave almost the same for all diameters. The intermediate values of velocities have approximately the same incrementation of force per diameter, but we can determine that 11.6 mm/s velocity has higher stiffness forces than the 7.8 mm/s.

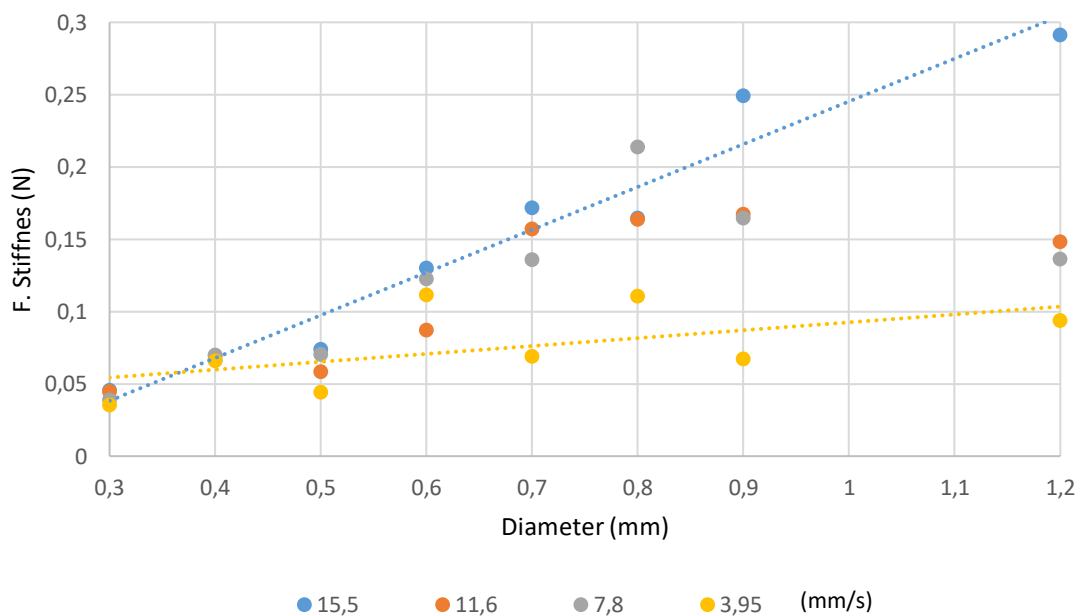


Figure 7.6 Stiffens Force, produced for each needle and feed velocity. [Own Source]

7.7.3. Cutting forces

In the following Figure 7.7, there are displayed the Maximum Cutting Force values for each test. In there we can see how these values increase with the increasing diameter. It is attributed to the deformations and stiffness force, to the increasing cutting area of each needle type. The unexpected results seen with these parameters were that the cutting forces incised for the smallest feed velocity, an average of 0.036 N, from the fastest velocity.

It may be the result of the tissue compression produced in the deformation process before the insertion, as the tissue layers in the 15.5 mm/s velocities was more compressed because of its higher stiffness force, then the forces needed afterward to cut these layers should be lower than the tests where the tissue was less compressed 3.95 mm/s. The comparison from the stiffness force to the cutting maximum force for a 1.2 mm diameter needle shows:

- An increase of force of 0.16 N for the 3.95 mm/s feed velocity.
- A decrease of 0.1 N for the 15.5 mm/s feed velocity.

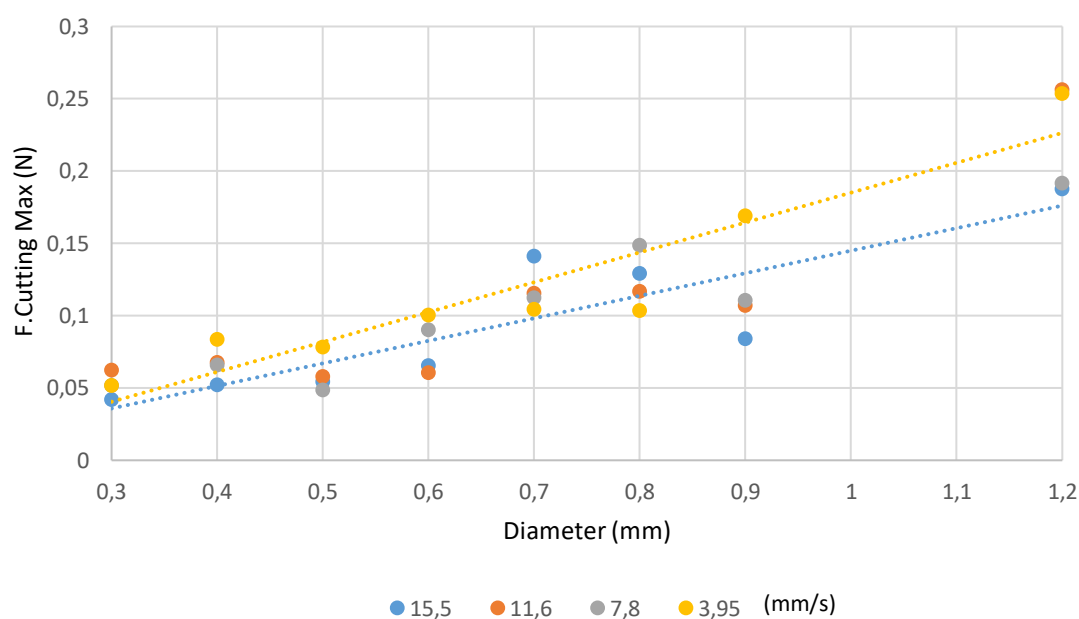


Figure 7.7 Maximum Cutting Force, produced for each needle and feed velocity. [Own Source]

The cutting forces represented on the following graph Figure 7.8 were extracted from the maximum cutting forces and the maximum depth penetrated. It shows an almost constant cutting force rate of the tissue between all tests, with an increasing tendency in the diameters, showing similar results than the graph before.

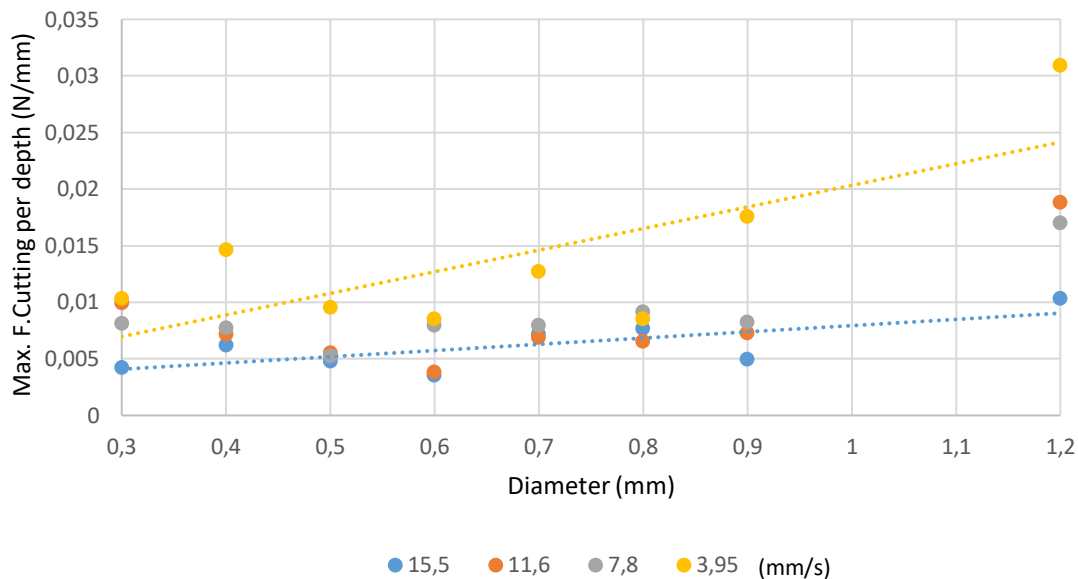


Figure 7.8 Cutting Force per depth, produced for each needle and feed velocity Tested. [Own Source]

7.7.4. Friction forces

Regarding the maximum friction forces displayed in Figure 7.9 shows how the increasing dimeters' influence the friction force, this is easily explained because of the increase of the needle perimeter, and the contact area between the needle and the tissue. Although it must be taken into account that the needle's contact surface not only depends on the diameter but on the length inserted. That is why it was decided to calculate the friction per contact is represented in the following Figure 7.10 and 7.11.

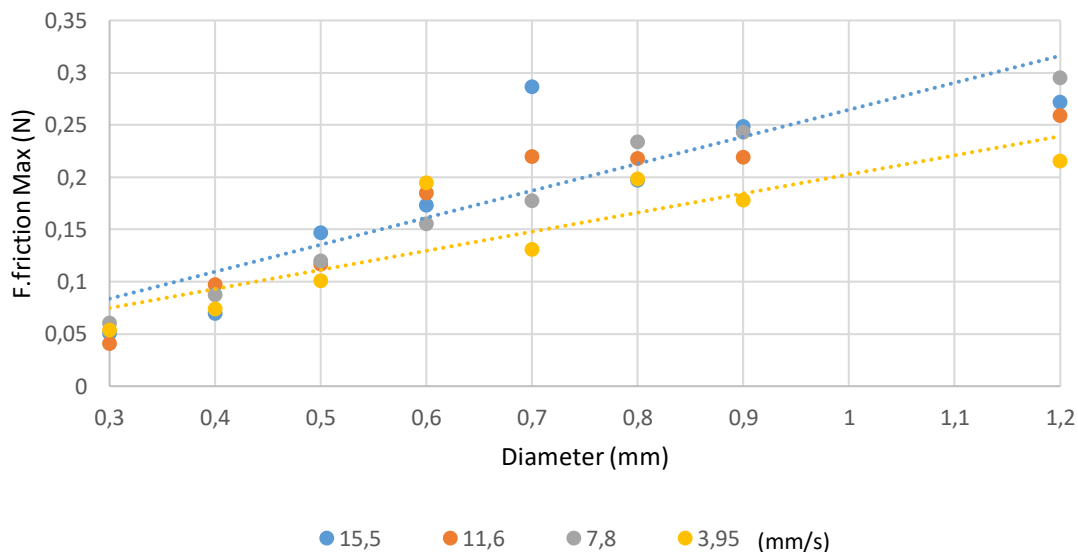


Figure 7.9 Maximum Friction Force, produced for each needle and feed velocity. [Own Source]

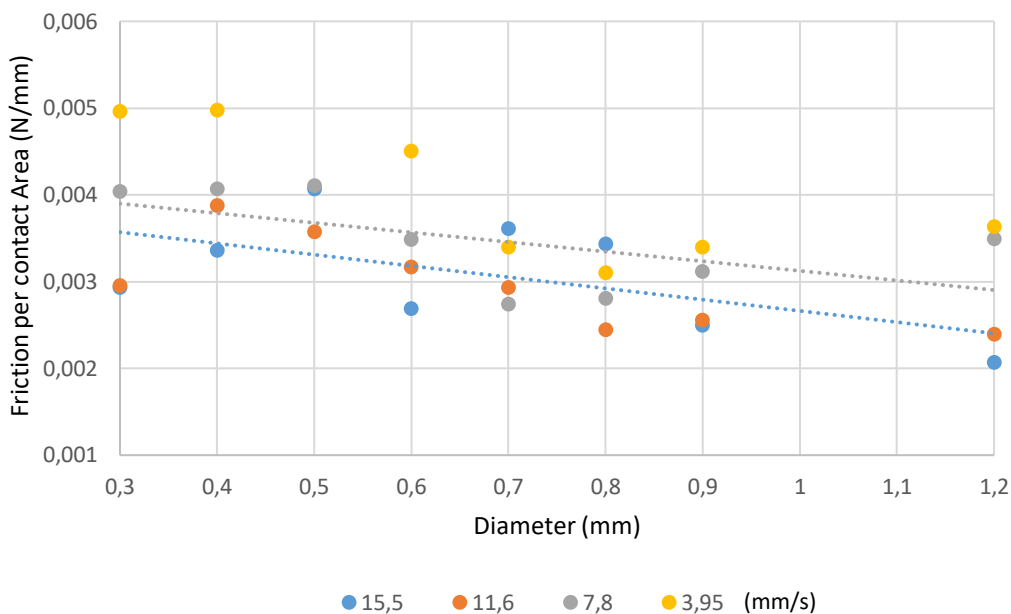


Figure 7.10 Friction per unit of contact area, produced for each needle and feed velocity [Own Source]

This parameter was calculated to extract some friction values independent from the depth of the needle penetrated, and it revealed some interesting information. It has been seen that for decreasing diameters, the friction forces per unit of contact area were almost constant, showing a decreasing tendency of friction forces for higher diameters. Figure 7.11 has a not expected behavior was for higher feed velocities, producing less friction force per area.

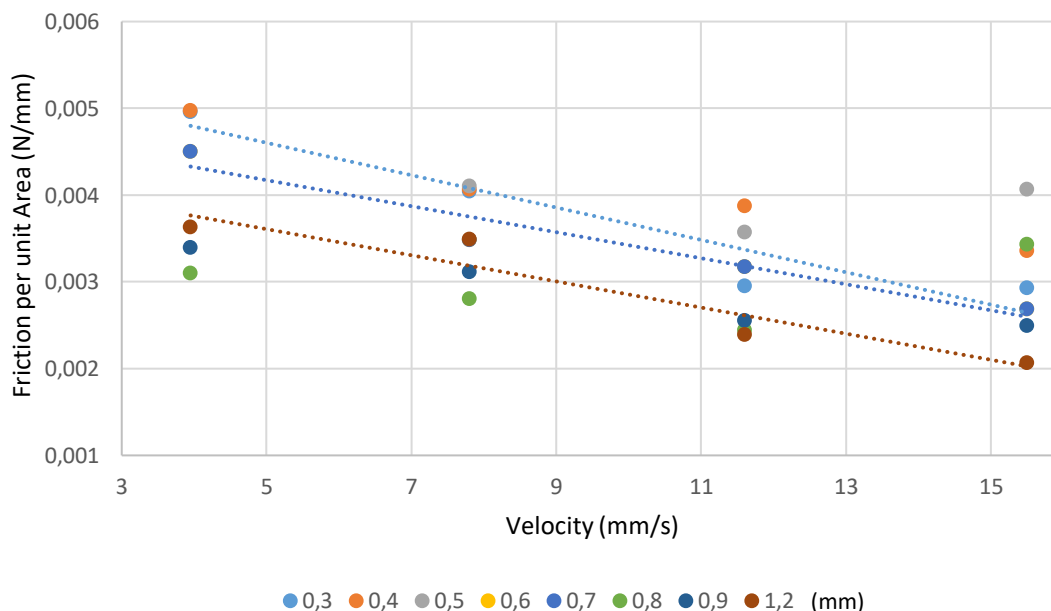


Figure 7.11 Friction per unit of contact area, produced for each needle and feed velocity [Own Source]

8. Discussion and Conclusions

8.1. Discussion

Based on the experimental results, we have captured the influence of the needle diameter and the insertion velocity on the needle insertion forces. In the following paragraphs are described the observations made of both parameters.

Diameter of the needle

Regarding the needle diameter, there is a clear correlation between the stiffness force increase and the increasing needle diameter. This trend is also found in the cutting forces and the friction forces, although in the friction force per area, besides remaining almost constant, in the results are denoted non-linear force decreases when bigger needle diameters are tested. The friction force increases until a certain point, where it changes its tendency despite the lineal increase of the needle diameter. This change of tendency is attributed to the creep and the relaxation of the tissue for a constant deformation over time, tests for larger needle diameters last longer than smaller ones and, consequently, the tissue relaxation is more visible in bigger diameters.

Insertion velocity

The insertion velocity has a straightforward influence on the insertion forces, increasing the forces to penetrate the soft-tissue when higher insertion velocities are used. The insertion velocity presents a more significant impact on the stiffness force than the needle diameter. The needle diameter influence is denoted for higher velocities, but for the lowest velocity, the diameter impact on the force is hardly visible.

An inverted behavior is appreciated in the cutting forces, for lower velocities the cutting forces displayed are higher than the ones when using higher velocities. However, the stiffness force and the deformation of the superficial layers increase when higher insertion velocities are employed. Therefore, the superficial soft-tissue layers tend to compress in an orderly fashion for lower insertion velocities, presenting a higher ultimate tensile strength. Whereas higher velocities tend to compress fewer layers, and consequently, a smaller ultimate tensile strength is denoted.

The insertion velocities also affect the friction forces per area, lower velocities produce higher friction forces. The slight decrease of the friction forces for higher velocities can be explained by the relaxation of the deformed material and the creep recovery.

8.2. Conclusions

The in-house prototype for this set of experiments has well accomplished all the requirements defined in the scope. It is exhibited that the selected range of load cell was accurate enough for the data acquisition, in terms of its sensitivity and sample rate. For the machine's driving part, it is accomplished the linear movement of the needle and its proper control, which can be modified easily with Arduino to test different insertion velocities. Although the vibrations should be controlled for each velocity, as the resonance speeds of the motor can be highly appreciated. The linear actuator's moving plate provides a wide range of testing opportunities due to the variability of plugins that can be added to the linear actuator. Additionally, the experimental methodology and data analysis employed are accurate regarding the requirements of these tests. All of them are subjected to further modifications, as the resulting methodologies and data analysis have been the result of multiple iterations, with the optimization of the calculus and procedures with the learnings of this first approach. There is no doubt in future works these will keep on changing and improving.

The output results from the experiments let us understand the complex needle insertion mechanism. It can be affirmed that this mechanism is not trivial due to the influence of the needle's geometry, the relative velocity of the needle while penetrating the tissue and the mechanical properties of the soft tissue. All these combined parameters present challenging research to optimize medical procedures with needles. Taking into consideration that it is used biological tissues, the results have a high dependency on its properties and composition that is not homogeneous in the entire material. This can explain the larger variability of the results, consequently, more experiments should be carried out to properly describe the influence of the operating parameters, refine the margin error, and ensure the mentioned tendencies.

8.3. Future Work

Despite the good preliminary results found between the deformations and the stiffness forces, further tests of the needle positioning should be done with a highspeed camera to register time and position, and properly determine the material deformation while being penetrated. More in-depth research will be done on testing different insertion velocities, needle diameters, and the characterization of the needle bevel tip. Besides the considerations above, it will be also considered the implementation of other relative movements to the needle as rotational or vibratory movements, and consequently the modification of the mechanical test bench. Finally, additional research tests are programmed with *Polyvinyl alcohol (PVA)* phantoms which mimic tissue samples, to provide the homogeneity that the biological tissues do not have to gather less dispersed results. Although for this study the mechanical properties of the sample should be previously analyzed.

9. Regulations and Environmental study

The regulations and Environmental study are together in this chapter because some of the regulations followed in this project are related to waste disposal and proper classification for correct waste treatment.

9.1. Regulations applied

All the legislations mentioned in this chapter have been somehow considered while building the machine and making the tests. It must be said that there might be some specifications not followed, as this project is a start point for this machine prototype and the experimental testing.

Considering the prototype manufactured as an industrial product, the current legislation applicable according to the Spanish legislation and *Fundación para el Fomento de la Innovación Industrial (FFII)* [30], is:

Machinery safety

- *Real Decreto 1644/2008, de 10 de Octubre* establishes the regulations regarding the commercialization and commissioning in machines (BOE 11.10.08) [31]

Low voltage machinery

- *Real Decreto 187/2016, de 6 de Mayo* regulates the safety requirements of electrical equipment intended for use in certain voltage limits (BOE 10.05.16) [32]

For the experimental tests carried out with biological ex-vivo tissues extracted from animals, there is Spanish legislation which regulates the good practices with animals for academic proposes:

Animal Protection

- *Real Decreto 53/2013, de 1 de Febrero* establishes the basic rules apply for the protection of animals used in experimentation and other scientific purposes, including academic purposes. [33]

There is specific national legislation for the electronic components wasted and their correct waste treatment. For the sanitary and biological waste produced, each Spanish region established the legislation, in this case, Catalunya.

Sanitary Waste

- *Decret 27/1999, de 9 de Febrer*, management of sanitary waste. [34]

Electronic Waste

- *Real Decreto 110/2015, de 20 de Febrero*, electrical and electronic components waste treatment (BOE 21.02.15) [35]

9.2. Environmental study

For the Environmental study of this project, it was done an approximation of the CO₂ emissions produced by the machines' electric consumption and the emissions produced in the shipping of the electronic components. The manufacturing emissions produced are included with the machine time of the parts manufactured in the University warehouse, but emissions produced on manufacturing the components bought are not included in the CO₂ emissions.

Shipment

Many electronic components of the machine were bought online via *Amazon and Banggood* to Chinese manufacturers. These components were shipped from China, using a distance calculator from a boat shipping company web page cold *Searates* [36], it was simulated a shipment from the Chinese city of Yantai to Barcelona, including the repartition truck distance, see Figure 9.2.

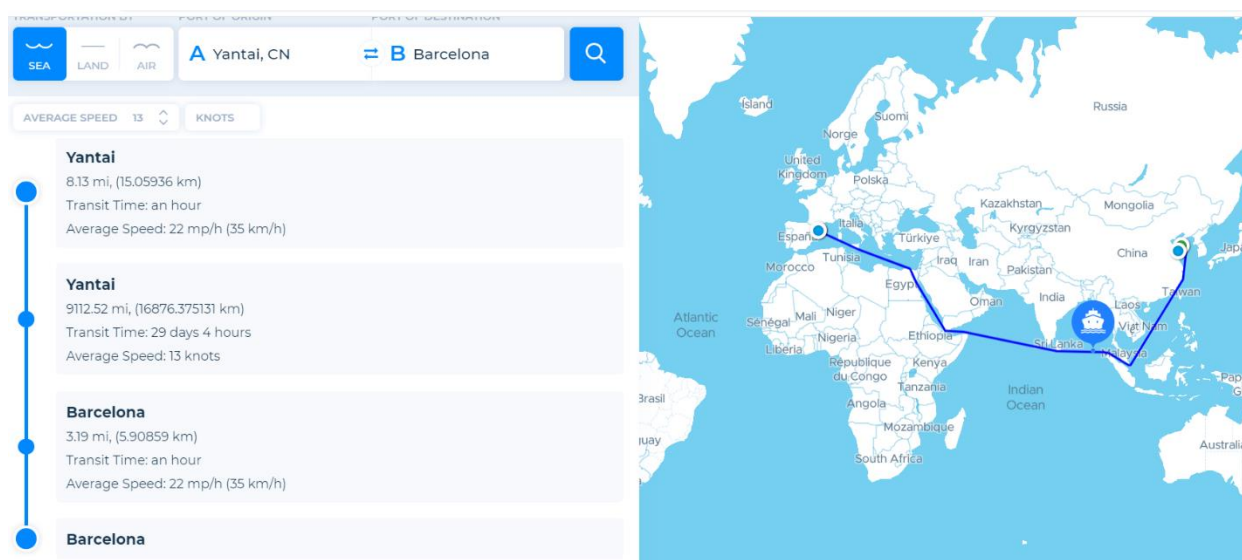


Figure 9.1 distances & time calculations of the Searates webpage. [36]

Once the shipment distance was found, it was proceeded to find the Carbon emissions produced per kg transported by the container vessel and the truck. According to an article found in [37], the

International Chamber of Shipping (ICS) published a comparison of CO₂ emissions between modes of transport shown below Figure 9.2

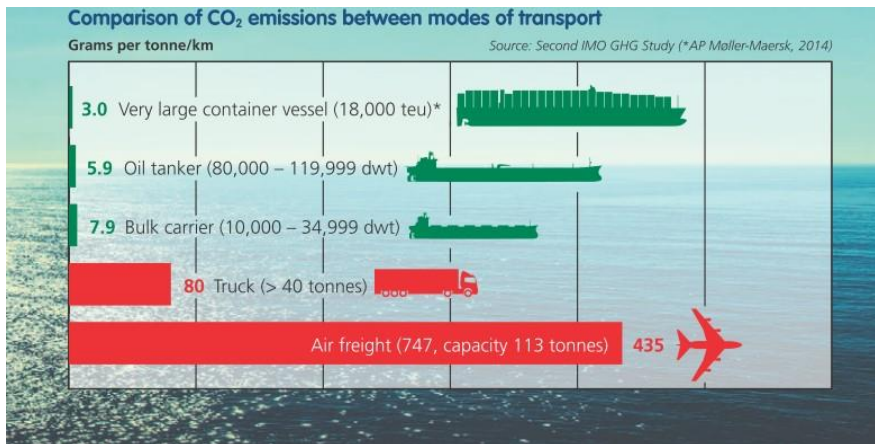


Figure 9.2 ICS. comparison of CO₂ emissions between modes of transport. [37]

It is calculated in Table 9.1 the Kg of CO₂ produced on the shipment of 10 kg package.

Table 9.1 CO₂ Kg produced by the shipment.

	Distance (Km)	CO ₂ (g) per ton/Km	CO ₂ (Kg)
Yantai (truck)	15	80	0.012
Yantai BCN (vessel)	16876.38	3	0.253
BCN (truck)	20.9	80	0.00836
TOTAL CO₂ (Kg)			0.273

Electric Consume

The machines' electric CO₂ production calculations used the milling machine's average usage hours and the electric consumption of the mechanical test bench while doing tests. The average CO₂ kg produced by KWh is extracted from the Spanish energy industry's average CO₂ emissions during 2019. All calculations are found in Table9.2.

Table 9.2 CO₂ Kg produced by the electric consume of the machines controlled.

	Work Hours (h)	Approximated Consume (kw/h)	Total Consume (Kw)	CO ₂ per kw produced (Kg Kw/h)	CO ₂ produced (kg)
Machine time	13	12	156	0.417305	65.09
Mechanic Bench	50	0.75	37.5		15.64
TOTAL CO₂					80.74

Total CO₂ produced

The total estimation of CO₂ produced by transportation, manufacturing controlled and testing electric consume are gathered in Table 9.3:

Table 9.3 Total CO₂ Kg produced.

	CO ₂ kg produced
Transportation	0.27
Electrical Consume	80.74
TOTAL	81.02

It can be appreciated that the CO₂ production calculated for the processes controlled is less than the CO₂ produced by an hour wash with a washing machine with 104.5Kg of CO₂ produced. However, this is not the overall calculation of the CO₂ produced because we do not have the emissions on the prebuilt parts. It can be said though, that the transportation of the components is much less polluting than the energy consumption of the machine build, and also it can be predicted that the machine manufacturing process, including the electronics manufacturing, is the most CO₂ polluting part of the project taking into consideration that the CO₂ production of the milling machine is by far more prominent than the electric consume of the prototype.

10. Project Budget

This project's budget is divided into 3 different cost modules: manufacturing cost, personnel cost, and the experimental trial cost.

10.1. Manufacturing cost

This budget details the prices for all the electronic components used in the project, specifying the price of the costumed protoboards made by the general services of UPC. It is also included elements and components materials bought for the structure. They are classified by the mechanical bench part they belonged, the load cell or linear actuator.

	Description	Price (€/unit)	Quantity	TOTAL (€)
Prefabricated Electronic components				
Load Cell	1kg load cell	9.45	1	9.45
	HX711 24-bit precision amplifier A/D sensor module	1.64	2	3.28
Linear	TB6600 42/57/86 Stepper Motor Controller	9.17	1	9.17
Actuator	HPV6 Linear module SFU12 04 Ball Screw Actuator line	151.59	1	151.59
	Zkee Shop 4A To 6A 24V Stable High Power Switching Power Supply AC-DC	11.99	1	11.99
	1pc IP66 Waterproof Connection Box of ELECTRONIC ABS Connection Project	10.89	1	10.89
	iLimate Grouper with Cable for RepRap Prusa Mendel CNC 3D Printer for Arduino Mega 2560 RAMPS 1.4 (6 Pack) KB01	10.99	1	10.99
	SODIAL(R) 3 Pin IEC320 C14 Input Module Plug Fuse Switch Plug Power Plug 10A 250V	3.56	1	3.56
	IEC320 C13 Power Cable for Cool Devices Printer, PC, Monitor, Television, Projector, 3 Pins, Black, 1.5m	8.99	1	8.99
	ELEGOO 17 Values 1% Resistor Set, 0 Ohm-1M Ohm (525 Pack)	9.34	1	9.34
	5Pcs 3 Pin Button Switch Emergency Stop Switch for Automation Equipment LA16-11ZS	10.19	1	10.19
	Coolty 125 V 6 A 3 Pins 2 Positions Mini Toggle Switch (10 Pieces) and Mini Momentary Pushbutton Switch (20 Pieces) Green/Red	13.99	1	13.99
	15 Assortment Units Assortment of 200-Piece Value Electrolytic Capacitors, Easy to Use	6.99	1	6.99
	DSD TECH HC-06 Bluetooth Wireless Serial Transceiver Support Module Slave Mode	2.99	1	2.99
Other	Roll wires tinned copper 30AWG P/N -30-1000	10.89	1	10.89

Other	3 x Nano Placa CH340/ATmega328P Compatible con Arduino IDE Proyecto Nano	13.99	1	13.99
	Goobay 40843 - Lead-free soldering tin; 1.0 mm, 17 g	9.19	1	9.19
	CNC kit with UNO+Shield+Stepper DRV8825 engine	45.03	1	45.03
Electronic Components Fabricated				
Protoboards	Load Cell Protoboard	14	1	14
	Linear Actuator Protoboard	14	1	14
Prefabricated Structural Components				
Machined	122 x 244 cm 3mm Transparent Finish Methacrylate Plates (PMMA)	1	27.22	27.22
Materials	4 X Clear Methacrylate Plate 8mm - Size 10 x 10cm	1	15	15
	Round aluminium tube 1000 x 10 mm	1	14.51	14.51
	Aluminium plate 70-75T6 15x150	1	23.7	23.7
	Steel sheets 0.5 mm thick	1	13.25	13.25
Threaded elements	Screw M5x20, grooved countersink head, nylon, DIN-963, 1 pc	5	0.21	1.05
	Screw STM32 5x12 - H3	1	0.5	0.5
Load Cell	Cylindrical screws with inner hexagon M8 x 30 mm (10 units)	1	11.5	11.5
	Phillips M5 x 16 stainless steel screws 304 flat head countersink screws (pack of 50)	1	8.77	8.77
	M3 x 20mm Phillips Nylon Hazelnut Head Bolt Black Machine Screw 50 pieces	1	9.52	9.52
Threaded elements	4 x 10 mm M4 cylindrical screws, steel, 20-unit package	1	10.78	10.78
Linear Actuator	Cylindrical screws with inner hexagon M6 x 30 mm (50 units)	1	17.06	17.06
TOTAL				523.37

10.2. Personnel cost

Personnel cost is separated from the machine assembly and the test one, because most of the professionals were involved in both. Here is included the price of the machine per hour for the manufactured components of the bench. Many components were manufactured at UPC warehouse, but the price specified belongs to an external company. The other two professionals specified in the budget, are the tutor of the project and the student. These two are specified the total hours spent in each task displayed in the chronogram found in the project Scope. It must be mentioned that the student cost per hour is calculated as if it was a junior mechanical engineer.

Professional	Price (€/h)	Total hours	TOTAL (€)
Senior Mechanical Engineer			
Machine Final Assembly	40	80	3200.00
Technical Documentation		8	302.86
Machine Calibrations		57	2285.71
Test Preparation		24	960.00
Needle Experimentation		8	320.00
Data Analysis		7	280.00
Memory Reviewing		50	2000.00
Junior Mechanical Engineer			
Arduino code learning	25	67	1666.67
Information search		40	1000.00
Machine Final Assembly		67	1666.67
Technical Documentation		120	3000.00
Machine Calibrations		53	1333.33
Test Preparation		40	1000.00
Needle Experimentation		8	200.00
Data Analysis		70	1750.00
Memory Writing		147	3666.67
Machine development			
Load cell electronics	60	6	360.00
Linear actuator		7	420.00
TOTAL			25,411.90

10.3. Experimental trials cost

In this budget is specified the tested needles' costs, biological samples and all materials used for the testing part of this project. It includes the price of 1kg of PVA bought to simulate a biological tissue that was finally not used.

Description	Price (€/unit)	Quantity	TOTAL (€)
Needles tested			
Hypodermic needle BD Microlance 0.5 mm x 16 mm. 25G X 5/8 Box of 100	2.54	1	2.54
Hypodermic needle BD Microlance 1,2 mm x 40 mm. 18G X 1 1/2 Box of 100	3.24	1	3.24
Hypodermic needle BD Microlance 0,9 m x 40 mm 20G x 1 1/2 Box of 100	2.54	1	2.54
BD Microlance Hypodermic Needle 0.8mm x 50mm 21G x 2. Box of 100	6.8	1	6.8
BD Microlance Hypodermic Needle 0.7mm x 40mm. 22G 1 1/2 Box of 100	2.75	1	2.75
BD Microlance Hypodermic Needle 0.3mm x 13mm. 30G 1/2 Box of 100	6.2	1	6.2
BD Microlance Hypodermic Needle 0.4mm x 13mm. 27G 1/2 Box of 100	3.63	1	3.63
BD Microlance 0.6mm x 25mm Hypodermic Needle. 23G X 1 Box of 100	2.54	1	2.54
Others			
5 Flat Plastic Glasses	0.95	2	1.9
Powder-free blue nitrile gloves. Size M. Box of 100u	12.9	1	12.9
Alcohol 96º 1000 ml	5	1	5
Chiken brests	4.25	1	4.25
341584 -1KG - POLY(VINYL ALCOHOL), 99+% HYDROLYZED	167	1	167
TOTAL			221.29

10.4. Total budget for manufacturing

It was calculated that the total manufacturing cost gathering the manufacturing budget with the personnel tasks assigned to this part of the project:

- Machine Time
- Machine Final Assembly
- Technical Documentation
- Machine Calibrations

Description	TOTAL (€)
Machine Manufacturing	523.37
Personnel	12,568.57
TOTAL	13,091.94

10.5. Total budget of the project

The following table lists the total cost of this project, including the manufacturing, personal and the cost for experimental trials.

Description	TOTAL (€)
Machine Manufacturing	523.37
Professionals	25,411.90
Tests	221.29
TOTAL	26,156.56

11. Bibliography

- [1] Shijian Zhao et al. "Trajectory Estimation of Flexible Needle Using PVA Tissue Material". 2019 IOP Conf. Ser.: Mater. Sci. Eng. 646 012063
- [2] B.H. Metklejohn. "The effect of rotation of an epidural needle". *AlioeJihwu*. 1987, Volume 42. pages 1180- 1182.
- [3] M. Scali , "P. Breedveld & D. Dodou. Experimental evaluation of a selfpropelling bio-inspired needle in single- and multi-layered phantoms". (2019) 9:19988.
- [4] Allison M. Okamura*, Member, IEEE, Christina Simone, and Mark D. O'Leary. "Force Modeling for Needle Insertion Into Soft Tissue". *IEEE TRANSACTIONS ON BIOMEDICAL ENGINEERING*, NO 10, VOL. 51, OCTOBER 2004
- [5] Robert J. Webster III, Jasenka Memisevic, and Allison M. Okamura. " Design Considerations for Robotic Needle Steering". *International Conference on Robotics and Automation Barcelona, Spain*, April 2005.
- [6] Youri RJ van Veen, Alex Jahya and Sarthak Misra. "Macroscopic and microscopic observations of needle insertion into gels". June 2012. DOI: 10.1177/0954411912443207 · Source: PubMed.
- [7] Mohsen Mahvash*, Member, IEEE, and Pierre E. Dupont, Senior Member, IEEE. "Mechanics of Dynamic Needle Insertion into a Biological Material". *IEEE TRANSACTIONS ON BIOMEDICAL ENGINEERING*, VOL. 57, NO. 4, APRIL 2010
- [8] Jiang, Shan; Li, Pan; Yu, Yan; Liu, Jun; and Yang, Zhiyong, "Experimental study of needle-tissue interaction forces: effect of needle geometries, insertion methods and tissue characteristics." (2014).
- [9] Seiji Aoyagi, Member, IEEE, Yutaka Takaoki, Hiroki Takayanagi, Chih-hao Huang, Takahiro Tanaka, Masato Suzuki, IEEE, Tomokazu Takahashi, IEEE, Tsutomu Kanzaki, Takuya Matsumoto. "Equivalent Negative Stiffness Mechanism Using Three Bundled Needles Inspired by Mosquito for Achieving Easy Insertion". 978-1-4673-1736-8/12/S31.00 ©2012 IEEE.
- [10] Fan Gao , Qinghua Song , Zhanqiang Liu , Yonghang Jiang and Xiuqing Hao. "Influence of a Biocompatible Hydrophilic Needle Surface Coating on a Puncture Biopsy Process for Biomedical Applications". *Coatings* 2020, 10, 178; doi:10.3390/coatings10020178
- [11] Marco Giovannini, Huaqing Ren , Xingsheng Wang , Kornel Ehmann "Tissue Cutting With Microserrated Biopsy Punches". Vol. 5, DECEMBER 2017. DOI: 10.1115/1.4037726.
- [12] Craig A Lehocky, Wendy Fellows-Mayle, Johnathan A Engh, Cameron N Riviere. "Tip design for safety of steerable needles for robot-controlled brain insertion". *Robotic Surgery: Research and Reviews* 2017:4 107–114.

- [13] Nikolai D.M. Begg, Alexander H. Slocum. "Audible frequency vibration of puncture-access medical devices". N.D.M. Begg, A.H. Slocum / Medical Engineering & Physics 36 (2014) 371–377.
- [14] Marco Giovannini, Huaqing Ren, Jian Cao and Kornel Ehmann," Study on design and cutting parameters of rotating needles for core biopsy, Journal of the Mechanical Behavior of Biomedical Materials", <https://doi.org/10.1016/j.jmbbm.2018.06.013>
- [15] Simon P. DiMaio, Student Member, IEEE, and S. E. Salcudean, Senior Member, IEEE." Needle Insertion Modeling and Simulation". IEEE TRANSACTIONS ON ROBOTICS AND AUTOMATION, VOL. 19, NO. 5, OCTOBER 2003
- [16] Winkler Foundation. [online] available on : [https://www.mae.ust.hk/~meqpsun/Notes/Chapter4\(202\).PDF](https://www.mae.ust.hk/~meqpsun/Notes/Chapter4(202).PDF)
- [17] A. BIOT, "Bending of an Infinite Beam on an Elastic Foundation"[online] available on:< <http://www.pmi.ou.edu/Biot2005/papers/FILES/029.PDF>>
- [18] <stanislave / Getty Images/iStockphoto>
- [19] J. Matthew Barnes, Laralynne Przybyla, and Valerie M. Weaver. "Tissue mechanics regulate brain development, homeostasis and disease". 2017. Published by The Company of Biologists Ltd | Journal of Cell Science (2017) 130, 71-82 doi:10.1242/jcs.191742
- [20] Biomechanics and Modeling of Skeletal Soft Tissues [online] available on : <https://www.researchgate.net/figure/Typical-stress-strain-curve-for-destructive-tensile-testing-of-skeletal-soft-tissues_fig3_221920273>
- [21] Wikipedia, Soft Tissues. [online] available on : <https://en.wikipedia.org/wiki/Soft_tissue#Mechanical_characteristics>
- [22] BME 332: Introduction to Biosolid Mechanics. Section 9: Ligament/Tendon Structure-Function. [online] available on: <http://umich.edu/~bme332/ch10ligten/bme332ligamenttendon.htm>
- [23] Orthopedic Bioengineering Research Laboratory at Colorado State University web page [online] available on: [Soft_Tissue_Viscoelasticity – OBRL \(colostate.edu\)](http://www.obrl.colostate.edu)
- [24] Zhengchu Tan a , Daniele Dini a, Ferdinando Rodriguez y Baena a , Antonio Elia Forte. "Composite hydrogel: A high fidelity soft tissue mimic for surgery". 0264-1275/© 2018 The Authors. Published by Elsevier Ltd. Article under the CC BY license (<http://creativecommons.org/licenses/by/4.0/>).
- [25] Mit App Inventor web page. [online] available on: < <https://appinventor.mit.edu/>>
- [26] HX711 Load Cell Transmitter Tutorial, Digital Balance. [online] available on: <https://www.naylampmechatronics.com/blog/25_tutorial-trasmisor-de-celda-decarga-hx711-ba.html>

- [27] Phyphox web page [online] available on: <<https://phyphox.org/>>
- [28] Gimp2 web page [online] available on: <<https://www.gimp.org/downloads/>>
- [29] Hypodermic Needles [online] available on: <https://en.wikipedia.org/wiki/Hypodermic_needle>
- [30] Fundación *para el Fomento de la Innovación Industrial (FFII)* web page [online] available on: <Productos industriales (f2i2.net)>
- [31] Real Decreto 1644/2008, de 10 de octubre, por el que se establecen las normas para la comercialización y puesta en servicio de las máquinas (BOE 11.10.08)
- [32] Real Decreto 187/2016, de 6 de mayo, por el que se regulan las exigencias de seguridad del material eléctrico destinado a ser utilizado en determinados límites de tensión (BOE 10.05.16)
- [33] Real Decreto 53/2013, de 1 de febrero, por el que se establecen las normas básicas aplicables para la protección de los animales utilizados en experimentación y otros fines científicos, incluyendo la docencia. BOE-A-2013-1337
- [34] Decret 27/1999, de 9 de febrer, de la gestió dels residus sanitaris. (DOGC núm. 2828 de 16/02/1999)
- [35] Real Decreto 110/2015, de 20 de febrero, sobre residuos de aparatos eléctricos y electrónicos (BOE 21.02.15)
- [36] Searates calculator [online] available on: <<https://www.searates.com/es/services/distances-time/>>
- [37] Article: ¿CUÁNTO CONTAMINA REALMENTE UN BUQUE? [online] available on: <<https://sectormaritimo.es/responsabilidad-medioambiental-eficiencia-del-transporte-maritimo>>